# Experimental characterization of material strain-rate dependence based on full-field Data-Driven Identification

Adrien Vinel, Rian Seghir, Julien Berthe, Gerald Portemont, Julien Réthoré

# Highlights

**Experimental characterization of material strain-rate dependence based on full-field Data-Driven Identification**

Adrien Vinel, Rian Seghir, Julien Berthe, Gérald Portemont, Julien Réthoré

- A Rate-dependent formulation of DDI is numerically and experimentally assessed
- Stress fields are identified within 11 % error beyond 100 MPa
- The monotonic high strain-rate dependent response of a mild steel is captured
- The yield stress and stress flow rate-dependence is identified up to 300 $s^{-1}$

# Experimental characterization of material strain-rate dependence based on full-field Data-Driven Identification

Adrien Vinel[a,b], Rian Seghir[a], Julien Berthe[b], Gérald Portemont[b], Julien Réthoré[a]

[a] *Nantes Universite Ecole Centrale Nantes CNRS GeM UMR 6183 F-44000 Nantes France*
[b] *DMAS ONERA F-59014 Lille France*

**Abstract**

This study experimentally explores the performances of a rate-dependent formulation of the Data-Driven stress Identification method for characterizing, using a single test, the monotonic high strain-rate dependent response of a mild steel alloy. First the Data-Driven Identification (DDI) method is presented in its rate-dependent form. A digital twin of a high speed tensile test performed on a notched sample geometry is then used to assess the performances of the DDI. It allows defining confidence intervals depending on multiple indicators (stress magnitude, multiaxiality...) and evaluate the range of strain-rate levels simultaneously captured. At last, the method is applied to a real experiment instrumented with High spatial Resolution Ultra High Speed camera (HR-UHS). The kinematic data are retrieved using Digital Image Correlation (DIC) then used as input for the DDI. Stress tensor fields are identified then the material rate-dependence retrieved and compared to the literature.


*Keywords:* DDI, High strain-rate, Ultra High Speed imaging, DIC, Digital twin

## 1. Introduction

Statically determinate test configurations, usually relying on homogeneous states of strain and stress, have historically been used to characterize the (thermo-) mechanical response of materials using a limited set of standardized sample geometries (*e.g.* dog-bone (1D), cruciform (2D)). In this context, both strain and stress, required to sample the material response, can be captured independently as scalar values from sensors in a purely experimental way. Such tests are usually thought as mono-parametric (*e.g.* constant strain-rate and temperature, uniaxial or in proportional loading) so a large number of test is required to sample a large loading space. In particular, some loading cases can not be properly analyzed or analyzed at all, including *e.g.* localization or dynamic transient processes where there is no more direct relationship between the measured external load and the stress distribution. Such limitations could be tackled using more complex geometries and/or loading conditions, *i.e.* carrying gradients (in space and/or time) and developing original inverse stress field identification methods relying on full-field imaging techniques such as Digital Image Correlation (DIC). Using the stress field itself as an unknown allows by-passing the use of an *a priori* constitutive equation to analyse such statistically indeterminate experiments, contrary to more standard inverse method such as Virtual Field Method (VFM), Finite-Element Model Updating (FEMU) which are parametric by nature. In that context, several strategies have been recently adopted to estimate heterogeneous stress fields without using a constitutive equation. All these strategies rely on full-field measurements and a regularization of the ill-posed mechanical problem, but they differ on the chosen regularization.

In 2014, Pierron and his co-authors [28] devised a strategy to estimate heterogeneous stress fields in dynamics (transient load) without using a constitutive law. The strategy relies on a one dimensional purely inertial configuration. Under the assumptions of plane stress, and a homogeneous and constant density of the material, the authors are able to estimate the mean stress field profile in the specimen. Here, the acceleration acquired experimentally acts as a 1D load cell, which requires recording the kinematic fields at ultra-high speed ($\geq 1$ Mfps). This work opened the way to a series of new standards: the Image-Based Inertial Impact (IBII) [11], Release (IBIR) [10] and Ultrasonic Shaking (IBUS) [34] tests. Among other things, the authors could eventually identify the elastic or viscoelastic modulus and tensile strength of brittle materials at high strain-rate. In these examples, the purely inertial and uniaxial nature of the test regularizes the problem.

In 2021, Liu *et al.* [24] and Cameron and his co-author [5] devised another strategy to estimate stress fields without postulating a constitutive equation. Assuming that the material is isotropic, the methods developed by these authors rely on the alignment of the principal directions of stress with strain or strain-rate. This assumption then

*Rian Seghir
*Email address:* rian.seghir@ec-nantes.fr (Rian Seghir)

allows obtaining a mathematically closed problem, and thus the analytical estimation of stresses. These methods have been tested on numerical example and experimentally in [24]. In [5], the authors discuss the range of validity of such an assumption: mainly in isotropic elasticity, plasticity with associative flow rules and for associative flow rules with an isotropic yield function. To the authors' knowledge, at this stage, this method cannot address the problem of elasto-plastic transition where stresses are not aligned with strains anymore and not aligned with plastic strain-rates yet.

A third kind of strategy was developed in the past 4 years: the so called Data-Driven approaches. These methods can be used to either solve the direct mechanical problem [18] (*i.e.* determining the displacement and stress distribution in a structure knowing the material response and boundary conditions), or the inverse mechanical problem [22] (*i.e.* determining some unobservable quantities or parameters from field measurements). The Data-Driven method were first introduced in the context of Computational Mechanics by Kirchdoerfer and Ortiz [18, 17] (DDCM). In their work, the authors replaced the constitutive equation by a minimization process and a material database. A solution to the direct problem is found by minimizing a distance between computed mechanical states (strains and stresses) and a set of admissible material states belonging to the database. Such a (strains and stresses) database can be built experimentally, using the inverse Data-Driven Identification (DDI) framework introduced in [22, 23]. This new problem aims to estimate stress fields, from experimental full-field measurements of displacement (and external load), without postulating any constitutive equation (contrary to *e.g.* VFM or FEMU). Using synthetic data, the authors demonstrated the ability of their algorithm to estimate stresses fields in homogeneous structures subjected to various loading cases (quasi-static and dynamic) and made of different class of material (hyper-elastic, elasto-plastic). It was recently extended numerically to heterogeneous (two-phase materials) hyper-elastic structures [37]. This Data-Driven method was then deployed experimentally by Dalémat *et al.* in [7]. In this study, perforated hyper-elastic membranes are submitted to uniaxial tensile tests. In a more recent paper [8] the authors extensively discuss the proper way to handle imperfect experimental data. They especially discussed boundary conditions issues for imperfectly defined edges and the way to tackle the issue of missing data. More recently, the Data-Driven strategy was applied by Langlois and his co-authors to address the topic of history dependent materials [19]. The use of this method enabled them to estimate stress fields during the formation of plastic instabilities such as Piobert-Lüders bands. In these strategies, the regularization comes from the assumption that the material response lies on a manifold in a constitutive space which is chosen *a priori*. The underlying hypothesis of this method will be presented later-on in this paper. Furthermore, one could imagine combining this method with the IBI methods in order to estimate heterogeneous 2D stress fields in transient dynamics without even needing load measurements. It has partly been demonstrated, on synthetic data, in [23].

These emergent strategies can potentially help to assess, without making any assumption, the validity of the current library of material constitutive equations outside their traditional calibration domain (*e.g.* introducing strain and strain rate heterogeneities, localization, multiaxiality) and to drastically reduce the number of tests required to characterize the behaviour of a material. The objective of this paper is to deploy a rate-dependent DDI formulation to characterize the yield stress and hardening rate-dependence of a mild steel using a single dynamic test. In that context, the DDI formulation and its resolution strategy will first be recalled. Then, a digital twin is built to investigate the ability of such a method and framework to estimate stress fields during our particular monotonic high strain-rate experiment, and to provide realistic error bars. At last, the DDI is applied to experimental data and the captured experimental rate-dependence is compared to literature.

## 2. Theoretical Framework

The inverse Data-Driven Identification method requires both, a rich database of displacement fields (obtained for example with DIC on complex sample geometries), and net external forces (usually obtained with a load cell). Combined with conservation laws (balance of linear and angular momentum), valid whatever the material, it is possible to build a minimization problem where the components of stress fields are the sought field variables. The following section guides the reader up to final formulation of the global minimization problem. To make the implementation clearer, we use in the following only matrix notation instead of tensorial one. By default, we use $[\bullet]$ for matrices and $\{\bullet\}$ for vectors. When indices are explicitly required they are emphasized as followed, $X_i^j$, where $i$ and $j$ are matrix rows and columns respectively. While the main ingredients are recalled in details we refer interested readers to [22] where the DDI problem was originally introduced. This work is also inspired by the works of Eggersmann and his co-authors [9] where a differential representation framework for DDCM, *i.e.* conditioning the material data set to short histories of stress and strain, was investigated. Furthermore, the modified strategy, regarding the initialization of the problem proposed in [23] is adopted. Some notations that will be recalled and used in this work were introduced by Langlois and his co-authors in [19]. The problem is formulated here in small strain, however, it has already been implemented and used in finite strain in [7, 29]. Moreover, for experimental concerns, we will focus only on plane-stress formalism.

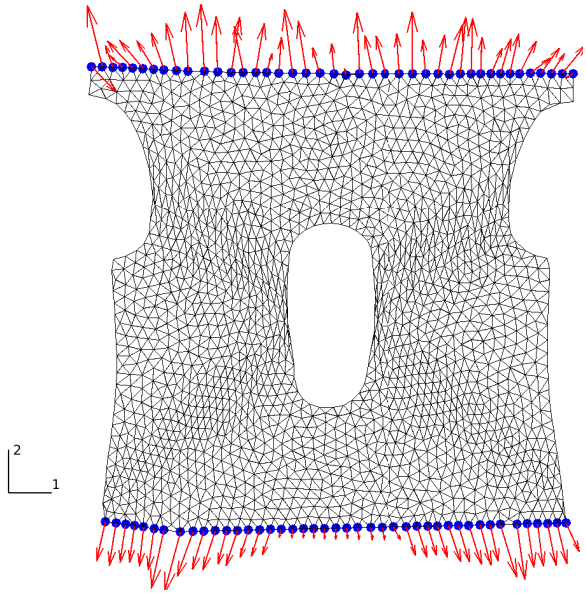


Figure 1: 2D deformable structure made of T3P1 elements over a domain $\Omega$. Blue bullets define the border $\partial F$ where loads and/or displacements are prescribed. Note that the upper part of the boundary $\partial F$ is named $\partial F^{up}$. Red arrows show a distribution of reaction or applied forces. The configuration is the one adopted for the digital twin (see Sec. 4) and the experimental investigation (see Sec. 5).

### *2.1. Static equilibrium problem*

The general problem considers a 2D structure made of a deformable continuum material (see Fig. 1). This structure is discretized using a Finite Element (FE) mesh with $N_e$ elements and $N_n$ nodes and the time history is discretized through $N_t$ time steps. Available data are the following:

- $[u]$: a $2N_n \times N_t$ matrix collecting nodal displacements obtained from DIC over the domain $\Omega$. The dimension $2N_n$ means that displacement vectors are organized in vector format such as $\{u^t\} = \{\mathcal{U}_1^t, ..., \mathcal{U}_n^t, \mathcal{V}_1^t, ..., \mathcal{V}_n^t\}$ where $\mathcal{U}$ and $\mathcal{V}$ are transverse (in the direction 1) and axial (in the direction 2) displacements respectively (see Fig. 1),

- $[B]$: a $3N_e \times 2N_n$ matrix obtained from the assembly of elementary FE gradient operators. The dimension $3N_e$ encloses the 3 components of the symmetric displacement gradient. It is computed using the mesh connectivity and relies on triangular elements and classical linear Lagrange shape functions. It allows for computing strain tensors at every quadrature points, here element centroids noted $e$. They are collected in a $3N_e \times N_t$ matrix:

$$[\boldsymbol{\varepsilon}] = [B]\,[u]\,. \tag{1}$$

- $[w]$: a $3N_e \times 3N_e$ diagonal matrix collecting the elementary integration weights times Jacobian determinants of the transformation of each element from its reference coordinates frame to its actual shape in the global undeformed coordinate system,

- $\{F\}$: a $N_t$ vector collecting the net force, along the axial direction 2 (see Fig. 1), of the nodal forces on the upper boundary $\partial F^{up}$:

$$\{F\} = b \sum_{k \in \partial F^{up}} f^t_{N_n+k} \quad \forall t \in [1, N_t], \tag{2}$$

with $b$ the thickness of the structure, supposed to be constant, and $[f]$ a $2N_n \times N_t$ matrix collecting the nodal internal forces. $N_n + k$ refers to axial displacements only, inline with displacement vector organization.

The discretized balance of momentum can therefore be expressed through a set of $N_t$ systems of $2N_n$ linear equations:

$$\begin{aligned} [B]^{\mathrm{T}}\,[w]^{\mathrm{T}}\,\{\boldsymbol{\sigma}^t\} &= \{f^t\}\,,\ \forall t \in [1, N_t], \\ \text{with} \sum_{k \in \partial F^{up}} f^t_{N_n+k} &= \frac{F^t}{e} \text{ and } f^t_k = 0,\ \forall k \in \Omega \backslash \partial F. \end{aligned} \tag{3}$$

Considering boundary conditions, especially the fact that only the net force along the axial direction 2 on $\partial F^{up}$ (see Fig. 1) is usually known in practice, and that displacements are prescribed everywhere else on $\partial F$, the set of $2N_n$ equations can be reduced to $\hat{N} = 2(N_n - \mathrm{card}(\partial F)) + 1$ equations. It is implemented by discarding from the system of equations (3) the degrees of freedom (DOF) associated to boundary nodes ($\partial F$) and by adding the constraint introduced in Eq. 2. It leads to the definition of new condensed operators $\left[\hat{B}\right]$ and $\left[\hat{f}\right]$ summarizing mechanical equilibrium into a compact form:

$$\left[\hat{B}\right]^{\mathrm{T}}\,[w]^{\mathrm{T}}\,\{\boldsymbol{\sigma}^t\} = \left\{\hat{f}^t\right\},\ \forall t \in [1, N_t] \tag{4}$$

### *2.2. Data-Driven Identification problem*

The main idea behind the DDI method consists in assuming that a constitutive equation exists, hence there is a constitutive space (still to be defined) where the whole set of mechanical states lies on a manifold. In short, among the infinity of solution of the static problem (see Eq. 4), one seeks for the one that minimizes the spread around an unknown manifold within a well defined constitutive space. Notice that in the following, such a manifold will be approximated by discrete points named material states, in the sense that they literally sample the material response in the constitutive space. Such a discretization allows for regularizing the ill-posed problem of stress identification as we will see later-on. As a consequence 3 main ingredients have to be defined: (1) such a "well defined" constitutive space, (2) a norm for estimating distances between states in

this potentially high dimensional constitutive space, and (3) the sampling of the manifold. The main assumptions of the method are enclosed in these three ingredients.

The constitutive space has to be chosen wisely regarding the various dependencies of the material response to observables and sought quantities. However, it does not necessarily have to match the "canonical" representation of the tested material class. Indeed, for example considering a purely mechanical response (stress *vs* strain evolution), a non-linear visco-elastic material cannot be distinguished from a visco-plastic one when submitted to a monotonic loading. An other example is proportional loading (monotonic or not). While history variable may be necessary for modelling purposes, in practice all material points with the same current strain state have experienced the same loading history and therefore, regardless of it, they respond similarly. In short, the constitutive space could be built only from strain and constitutive variables which are not colinear to strain in the particular tested loading scenario. To the authors' knowledge, a proper theoretical investigation of the constitutive space representation in DDI has not been proposed yet and it goes way beyond the scope of the present paper. Since we will focus on monotonic and proportional loading applied to a rate-dependent material we will use in the following a first order differential approach as proposed in [9] for non-linear visco-elastic material. The validity of this framework for our particular experimental case will be checked later-on numerically, using a digital twin in Sec. 4 and then experimentally in Sec. 5 by comparing the identified material response with uniaxial test data from the literature. In that framework, the material response is only described using strain, stress and their first order time derivatives. In practice, and similarly to what is done in [19], an incremental approach will be used, leading to a dependence of the current stress to the current strain and the former strain and stress:

$$\boldsymbol{\sigma}^t = \tilde{\sigma}^t \left( \boldsymbol{\varepsilon}^t, \boldsymbol{\varepsilon}^{t-1}, \tilde{\boldsymbol{\sigma}}^{t-1} \right). \tag{5}$$

$\tilde{\sigma}$ will be further used as the DDI estimation of the actual stress in this particular space. Then, let us define a distance in a strain and stress tensor related constitutive space. Following [18] we choose a norm built from a symmetric positive definite fourth-order tensor $\mathbb{C}_o$. Noting for example $\{\mathcal{P}^t\}$ and $\{\mathcal{Q}^t\}$, two vectors related to some strain and stress tensorial quantities at time $t$ respectively in Voigt notation, an energetic $\|\|^2_{\mathbb{C}_o}$ norm can be introduced as follows:

$$\|\mathcal{P}^t, \mathcal{Q}^t\|^2_{\mathbb{C}_o} = \left\{\mathcal{P}^t\right\}^{\mathrm{T}} \left[\mathbb{C}_o\right] \left\{\mathcal{P}^t\right\} + \left\{\mathcal{Q}^t\right\}^{\mathrm{T}} \left[\mathbb{C}_o\right]^{-1} \left\{\mathcal{Q}^t\right\}. \tag{6}$$

Normalizing data, such as:

$$\begin{aligned} \left\{\underline{\mathcal{P}}^t\right\} &= \left[\sqrt{\mathbb{C}_o}\right] \left\{\mathcal{P}^t\right\}, \\ \left\{\underline{\mathcal{Q}}^t\right\} &= \left[\sqrt{\mathbb{C}_o}\right]^{-1} \left\{\mathcal{Q}^t\right\}, \end{aligned} \tag{7}$$

the norm simply becomes:

$$\|\mathcal{P}^t, \mathcal{Q}^t\|^2_{\mathbb{C}_o} = \left\{\underline{\mathcal{P}}^t\right\}^{\mathrm{T}} \left\{\underline{\mathcal{P}}^t\right\} + \left\{\underline{\mathcal{Q}}^t\right\}^{\mathrm{T}} \left\{\underline{\mathcal{Q}}^t\right\}. \tag{8}$$

Notice that the square root of the tensor $[\mathbb{C}_o]$ is computed using an eigen value decomposition, $\left[\sqrt{\mathbb{C}_o}\right] = [V]\left[\sqrt{D}\right][V]^{\mathrm{T}}$, where $[V]$ and $[D]$ are matrices containing eigen vectors and eigen values respectively. Such a normalization will help being more generic, especially avoiding being intrusive for the clustering part of the problem (see Sec. 2.4).

As introduced above, to address the issue of ill-posedness of the stress field identification problem, the material response is discretized with a finite set of $N^*$ unknown material states $(\{\boldsymbol{\varepsilon}^*\}, \{\boldsymbol{\varepsilon}^{**}\}, \{\boldsymbol{\sigma}^*\}, \{\boldsymbol{\sigma}^{**}\})$, where $\bullet^*$ are related to the current state and $\bullet^{**}$ to the former state. We will see that these $N^*$ states are in practice defined as barycenters of mechanical state clusters. These clusters regroup the set of strains and sought stresses $\left(\{\boldsymbol{\varepsilon}^t\}, \{\boldsymbol{\varepsilon}^{t-1}\}, \{\tilde{\boldsymbol{\sigma}}^t\}, \{\tilde{\boldsymbol{\sigma}}^{t-1}\}\right)$ that are close in the $\|\|^2_{\mathbb{C}_o}$ norm.

Considering the constitutive space introduced in Eq. 5, the norm introduced in Eq. 8 and the sampling of the material response into $N^*$ current and former states, the problem can be formulated as a global minimization:

$$\min_{\substack{\boldsymbol{\varepsilon}^* \boldsymbol{\varepsilon}^{**} \tilde{\boldsymbol{\sigma}} \\ \boldsymbol{\sigma}^* \boldsymbol{\sigma}^{**} \mathcal{S}}} \Psi\left(\boldsymbol{\varepsilon}, \boldsymbol{\varepsilon}^*, \boldsymbol{\varepsilon}^{**},\ \tilde{\boldsymbol{\sigma}}, \boldsymbol{\sigma}^*, \boldsymbol{\sigma}^{**}, \mathcal{S}\right), \tag{9}$$

where

$$\Psi = \frac{1}{2} \sum_{t=2}^{N_t} \left( \|\mathcal{P}^t, \mathcal{Q}^t\|^2_{\mathbb{C}_o} + \|\mathcal{P}^{t-1}, \mathcal{Q}^{t-1}\|^2_{\mathbb{C}_o} \right), \tag{10}$$

with

$$\begin{aligned} \underline{\mathcal{P}}^t &= \left[\sqrt{p^t}\right] \left( \left\{\underline{\boldsymbol{\varepsilon}}^t\right\} - \left[\mathcal{S}^t\right] \left\{\underline{\boldsymbol{\varepsilon}}^*\right\} \right), \\ \underline{\mathcal{P}}^{t-1} &= \left[\sqrt{p^{t-1}}\right] \left( \left\{\underline{\boldsymbol{\varepsilon}}^{t-1}\right\} - \left[\mathcal{S}^t\right] \left\{\underline{\boldsymbol{\varepsilon}}^{**}\right\} \right), \\ \underline{\mathcal{Q}}^t &= \left[\sqrt{p^t}\right] \left( \left\{\underline{\tilde{\boldsymbol{\sigma}}}^t\right\} - \left[\mathcal{S}^t\right] \left\{\underline{\boldsymbol{\sigma}}^*\right\} \right), \\ \underline{\mathcal{Q}}^{t-1} &= \left[\sqrt{p^{t-1}}\right] \left( \left\{\underline{\tilde{\boldsymbol{\sigma}}}^{t-1}\right\} - \left[\mathcal{S}^t\right] \left\{\underline{\boldsymbol{\sigma}}^{**}\right\} \right), \end{aligned} \tag{11}$$

under the constraint that the equilibrium equations (Eq. 4) are satisfied. $[p]$ is a $3N_e \times 3N_e \times N_t$ matrix weighting mechanical states contributions for every time-steps within the functional $\Psi$. A specific section (see Sec. 2.5) is dedicated later-on to address the role of these weights. $[\mathcal{S}]$ is a $3N_e \times 3N^* \times N_t$ selection matrix that maps the $N^*$ material states to the mechanical states for every time-steps. Eq. 9 must be understood as the global minimization (time and

space) of the scattering of mechanical states around their associated $N^*$ material states (barycenters) in the particular constitutive space $(\boldsymbol{\varepsilon}^t, \boldsymbol{\varepsilon}^{t-1}, \tilde{\boldsymbol{\sigma}}^t, \tilde{\boldsymbol{\sigma}}^{t-1})$. If equilibrium constraints are enforced using Lagrange multipliers, the following cost function can be obtained:

$$\Phi = \Psi + \sum_{t=1}^{N_t} \left( \left[\underline{\hat{B}}\right]^{\mathrm{T}} [w]^{\mathrm{T}} \left\{\underline{\tilde{\boldsymbol{\sigma}}}^t\right\} - \left\{\hat{f}^t\right\} \right) \left\{\lambda^t\right\} \quad \forall t \in [1, N_t]. \tag{12}$$

Notice that the introduction of normalized quantities "$\underline{\bullet}$" also requires the normalization of $\hat{B}$ with $[\mathbb{C}_o]$. It is simply done by assembling normalized gradient operators. Finally, two problems can be formulated: (1) the *mechanical problem* and (2) the material one. The stationarity of $\Phi$ with respect to $\{\lambda^t\}$ and $\left\{\tilde{\underline{\sigma}}^t\right\}$ leads to the *mechanical problem* and the following set of $N_t$ systems of $3N_e \times \hat{N}$ equations:

$$\begin{bmatrix} \left[\underline{\hat{B}}\right]^{\mathrm{T}} [w]^{\mathrm{T}} & 0 \\ \alpha^t & [p^t]^{-1} [w] \left[\underline{\hat{B}}\right] \end{bmatrix} \begin{Bmatrix} \tilde{\underline{\boldsymbol{\sigma}}}^t \\ \lambda^t \end{Bmatrix} = \begin{Bmatrix} \hat{f}^t \\ D^t \end{Bmatrix}, \tag{13}$$

with

$$\alpha^t = \begin{cases} 1 & \forall t \in [1, N_t], \\ 2 & \forall t \in [2 : N_{t-1}], \end{cases}$$

$$\left\{D^t\right\} = \begin{cases} \left[\mathcal{S}^{t+1}\right] \left\{\underline{\sigma}^{**}\right\} & t = 1, \\ \left[\mathcal{S}^{t+1}\right] \left\{\underline{\sigma}^{**}\right\} + \left[\mathcal{S}^t\right] \left\{\underline{\sigma}^*\right\} & \forall t \in [2 : N_{t-1}], \\ \left[\mathcal{S}^t\right] \left\{\underline{\sigma}^*\right\} & t = N_t. \end{cases} \tag{14}$$

Then, the stationarity with respect to the material states leads to the *material problem* resulting in 4 sets of $3N^*$ equations:

$$\begin{cases} \sum\limits_{t=2}^{N_t} \left[\mathcal{S}^t\right]^{\mathrm{T}} [p^t] \left[\mathcal{S}^t\right] \left\{\underline{\boldsymbol{\varepsilon}}^*\right\} & = \sum\limits_{t=2}^{N_t} \left[\mathcal{S}^t\right]^{\mathrm{T}} [p^t] \left\{\underline{\boldsymbol{\varepsilon}}^t\right\}, \\ \sum\limits_{t=1}^{N_{t-1}} \left[\mathcal{S}^{t+1}\right]^{\mathrm{T}} [p^t] \left[\mathcal{S}^{t+1}\right] \left\{\underline{\boldsymbol{\varepsilon}}^{**}\right\} & = \sum\limits_{t=1}^{N_{t-1}} \left[\mathcal{S}^{t+1}\right]^{\mathrm{T}} [p^t] \left\{\underline{\boldsymbol{\varepsilon}}^t\right\}. \end{cases} \tag{15}$$

Similar equations are used for $\{\underline{\sigma}^*\}$ and $\{\underline{\sigma}^{**}\}$ respectively. Stationarity with respect to $[\mathcal{S}^t]$, to update the state mapping, is difficult to explicit. Indeed, contrary to other variables, which are continuous numbers of $\mathbb{R}$, $[\mathcal{S}]$ is made of integers in $\mathbb{N}$. As a consequence, an alternative method is employed. Details are given in Sec. 2.4. The resolution of such a problem has already been discussed in [23, 35]. It relies on a staggered algorithm that computes alternatively the Lagrange multipliers and the correction of the stress fields for a given material state set and selection matrix (called the *mechanical problem*), then the update of the material states set and selection matrix for given stresses (called the *material problem*). These two steps are discussed in the next sections.

### 2.3. Resolution of the mechanical problem

Let us consider a given set of material states: $(\{\underline{\boldsymbol{\varepsilon}}^*\}, \{\underline{\boldsymbol{\varepsilon}}^{**}\}, \{\underline{\boldsymbol{\sigma}}^*\}, \{\underline{\boldsymbol{\sigma}}^{**}\})$ and a given mapping through the selection matrix $[\mathcal{S}]$. The *mechanical problem* can be solved by substitution, leading first to the computation of the Lagrange multipliers:

$$\underbrace{\left[\underline{\hat{B}}\right]^{\mathrm{T}} [w]^{\mathrm{T}} \left[p^t\right]^{-1} [w] \left[\underline{\hat{B}}\right]}_{[\mathcal{M}^t]} \left\{\lambda^t\right\} = \underbrace{\left[\underline{\hat{B}}\right]^{\mathrm{T}} [w]^{\mathrm{T}} \left\{D^t\right\} - \alpha^t \left\{\hat{f}^t\right\}}_{\{b^t\}} \quad \forall t \in [1, N_t]. \tag{16}$$

It consists in a set of $N_t$ systems of $\hat{N}$ independent linear equations to solve. Finally, stresses are updated using the second line of the system of equations 13:

$$\left\{\tilde{\underline{\boldsymbol{\sigma}}}^t\right\} = \frac{1}{\alpha^t} \left( \left\{D^t\right\} - \left[p^t\right]^{-1} [w] \left[\underline{\hat{B}}\right] \left\{\lambda^t\right\} \right), \forall t \in [1, N_t]. \tag{17}$$

### 2.4. Resolution of the material problem

First, the mapping operator, *i.e.* $[\mathcal{S}]$, must be computed for given stress fields and the actual set of material states. Finding for each element $e$ the material state $N_i^*$ that is the closest with respect to $\|\|^2_{\mathbb{C}_o}$ is done using the k-d tree method. Indeed, since for each iteration of the *material problem* the database of material state is fixed, efficient space-partitioning data structure strategy can be used to strongly accelerate this operation which remains the bottleneck of the method. Once this matrix is obtained, the set of material states $(\{\underline{\boldsymbol{\varepsilon}}^*\}, \{\underline{\boldsymbol{\varepsilon}}^{**}\}, \{\underline{\boldsymbol{\sigma}}^*\}, \{\underline{\boldsymbol{\sigma}}^{**}\})$ is updated using Eq. 15. The complexity of the resolution mainly depends on the form of $[p^t]$. If $[p^t]$ is diagonal, as it has always been the case in the literature according the authors' knowledge, the resolution of Eq. 15 simply consists in computing $5 \times 3N^*$ independent averages or weighted averages of the mechanical states in elements assigned to each material states through $[\mathcal{S}]$. For example current and former material strains are found such as:

$$\begin{cases} \underline{\boldsymbol{\varepsilon}}_i^* = & \dfrac{\sum\limits_{t=2}^{N_t} \sum\limits_{j=1}^{3N_e} \left(\mathcal{S}_j^i\right)^t \left(p_j^k\right)^t \underline{\boldsymbol{\varepsilon}}_k^t}{\sum\limits_{t=2}^{N_t} \sum\limits_{k=1}^{3N_e} \sum\limits_{j=1}^{3N_e} \left(\mathcal{S}_j^i\right)^t \left(p_j^k\right)^t \left(\mathcal{S}_k^l\right)^t} \\ \underline{\boldsymbol{\varepsilon}}_i^{**} = & \dfrac{\sum\limits_{t=1}^{N_t-1} \sum\limits_{j=1}^{3N_e} \left(\mathcal{S}_j^i\right)^{t+1} \left(p_j^k\right)^t \underline{\boldsymbol{\varepsilon}}_k^t}{\sum\limits_{t=1}^{N_t-1} \sum\limits_{k=1}^{3N_e} \sum\limits_{j=1}^{3N_e} \left(\mathcal{S}_j^i\right)^{t+1} \left(p_j^k\right)^t \left(\mathcal{S}_k^l\right)^{t+1}} \\ & \forall i \in [1 : 3N^*]. \end{cases} \tag{18}$$

The next section discusses the choice of such a weighing matrix $[p^t]$.

### 2.5. Choice of a weighing matrix

The weighing matrix $[p]$ of the elementary distance between one mechanical state and its corresponding material state, introduced in the DDI norm (see Eq. 8), can

be wisely used as a natural filter for noisy experimental inputs. Inputs of the DDI being itself an output of the DIC inverse problem, it is necessarily biased and corrupted by noise. Finding a way to mitigate this issue could be valuable for the application of the DDI method to real experimental data. Some solutions have already been proposed in the literature for such a weighting matrix. Even if it has not been explicitly written as such in literature, two cases can be found: $[p^t] = \mathbf{I}_2$, the identity matrix, or $[p^t] = [w]$ (see *e.g.* [19]). The first solution gives an equal weight to each element, each tensor component and each time-step. The authors found it useful when the objective is to identify stresses in vicinity of a localization band using a strongly refined mesh. Indeed, the second option, classical for FE integrals, gives more weight to large and undistorted elements then reducing the contribution of data in the refined mesh areas where strain localization is expected/observed. Alternative routes could be used, designing a weighting matrix enabling the minimization, for example, of the stress identification noise but this is out-of-the scope of this work. In the following, only the two above mentioned cases will be compared.

### *2.6. Schematic of the global minimization problem*

The resolution of the problem, *i.e.* computing $(\{\underline{\boldsymbol{\varepsilon}}^*\}, \{\underline{\boldsymbol{\varepsilon}}^{**}\}, \{\underline{\boldsymbol{\sigma}}^*\}, \{\underline{\boldsymbol{\sigma}}^{**}\})$, $[\underline{\tilde{\boldsymbol{\sigma}}}]$ and $[\mathcal{S}]$, is performed using the following staggered algorithm [19]:

1. initialize $[\underline{\tilde{\boldsymbol{\sigma}}}]$ using a FE simulation with an arbitrary model,
2. normalize input dataset to get $([\underline{\tilde{\boldsymbol{\sigma}}}], [\underline{\boldsymbol{\varepsilon}}])$,
3. initialize $(\{\underline{\boldsymbol{\varepsilon}}^*\}, \{\underline{\boldsymbol{\varepsilon}}^{**}\}, \{\underline{\boldsymbol{\sigma}}^*\}, \{\underline{\boldsymbol{\sigma}}^{**}\})$ and $[\mathcal{S}]$ using a k-means algorithm [25] on $\left(\{\underline{\boldsymbol{\varepsilon}}^t\}, \{\underline{\boldsymbol{\varepsilon}}^{t-1}\}, \{\underline{\tilde{\boldsymbol{\sigma}}}^t\}, \{\underline{\tilde{\boldsymbol{\sigma}}}^{t-1}\}\right) \forall t \in [1, N_t]$,
4. solve the *mechanical problem* (see Sec. 2.3),
5. solve the *material problem* (see Sec. 2.4), eventually using k-d tree. This step is iterated until convergence of $[\mathcal{S}]$. It usually takes less than 3 iterations to converge,
6. iterate steps 4 through 5 until convergence of $[\mathcal{S}]$ and $[\underline{\tilde{\boldsymbol{\sigma}}}]$.

### *2.7. Algorithmic parameters*

Once the framework of the DDI method is set, meaning that a particular constitutive space (see Eq. 5) and a particular norm (see Eq. 8) are selected, 5 parameters remain to be adjusted by the user and will affect performances of the algorithm. (1) the number of material states $N^*$ sampling the material response, (2) the amplitude and the exact form of $\mathbb{C}_o$, (3) the two convergence criteria and (4) the weighing matrix $[p]$. The first one and part of the second has already been investigated by Dalémat and her co-authors in [8] using FE reference solutions and varying the number of DDI material states. They concluded that a small number of material states leads to an insufficient sampling of the strain-stress manifolds while a high number of material states allows outliers to develop and increases the sensitivity to noise (similarly to the overfitting phenomenon for regressions). The authors proposed the following rule of thumb for choosing $N^*$: $20 \leq \frac{(N_t-1)\cdot N_e}{N^*} \leq 100$, where the numerator is the experimental database size. The influence of the magnitude of $\mathbb{C}_o$ was found to be straightforward as it only intervenes for the clustering step. Eq. 7 shows that by choosing a tensor with high values, the normalization will give more weight to strains compared to stresses. So, for the robustness of the clustering, it may be relevant to use a $\mathbb{C}_o$ of high amplitude in order to give more weight to strains which are obtained experimentally, compared to stresses which are unknown and which are continuously changing during the minimization process. To the authors' knowledge, the question of the influence of the symmetry of $\mathbb{C}_o$ has not been investigated yet and it is not the objective of the present work. In the following, a pseudo Hooke tensor for an isotropic material is used. Its definition only depends on a pseudo-Young modulus $E_o$ (the magnitude) and pseudo-Poisson ratio $\nu_o$. Regarding the two convergence criteria, one uses for the *material problem* the convergence rate of the data-driven distance $\Psi$ (see Eq. 9) at each iteration $i$. That is to say:

$$\frac{|\Psi_i - \Psi_{i-1}|}{\Psi_0} \geq \epsilon_{mat}, \tag{19}$$

where $\Psi_0$ is its initial value and $\epsilon_{mat}$ the user criterion. For the *mechanical problem*, we use the convergence rate of the sum (space/time) of the norm of internal force vectors (See Eq. 4). That is to say:

$$\frac{|\mathcal{F}_i - \mathcal{F}_{i-1}|}{|\mathcal{F}_0|} \geq \epsilon_{mech}, \text{ with } \mathcal{F} = \sum_{t=1}^{N_t} \sum_{e \in \Omega} |\, [\underline{B}]^{\mathrm{T}} [w]^{\mathrm{T}} \left\{\underline{\tilde{\boldsymbol{\sigma}}}^t\right\} |^2. \tag{20}$$

Notice that it is not necessarily equal to zero due to the slight difference between Eq. 12 (where we impose equilibrium through Lagrangian multipliers) and Eq. 4 where $[\underline{B}]$ is used instead of $\left[\underline{\hat{B}}\right]$. Indeed, the equilibrium of the structure is imposed using $\hat{B}$, *i.e.* only in an integral manner over $\partial F^{up}$. So the convergence of Eq. 20 reflects the convergence of the load profile. Regarding the weighing matrix two options will be compared in this paper:

$\mathcal{H}_0$: $[p^t] = \mathbf{I}_2$, $\forall t \in [1, N_t]$,
$\mathcal{H}_1$: $[p^t] = [w]$.

Table 1 summarizes the inputs, outputs, parameters and assumptions needed for the proposed Data-Driven Identification method. It emphasizes the fact that, evenif DDI presents itself as a model-free technique for fields of stress tensors estimation, part of the modelling framework is hidden in the choice of the constitutive space. Nevertheless, while the framework is constrained, the exact form of the constitutive equation remains free. Moreover, the role of user parameters remains significant and many aspects still have to be investigated.

| Inputs | Outputs | Parameters | Assumptions |
|---|---|---|---|
| $[u_{\text{dic}}], \{F\}$ | $[\mathcal{S}]$ | $\mathbb{C}_o$ | Plane stress |
| $[B]$ | $[\tilde{\boldsymbol{\sigma}}]$ | $N^*$ | Small strain |
| $[\boldsymbol{\sigma}_{\text{fe}}]$ | $\{\boldsymbol{\varepsilon}^*\}, \{\boldsymbol{\varepsilon}^{**}\}$ | $\epsilon_{mat}, \epsilon_{mech}$ | Constitutive space |
| | $\{\sigma^*\}, \{\sigma^{**}\}$ | $[p]$ | |
| | $\Psi$ | | |

Table 1: Summary of the inputs, outputs, parameters and the assumptions needed for the Data-Driven Identification method proposed in this work. In this table, $\Psi$ gives the DDI distance at convergence providing information about the compactness of the identified mechanical states around a manifold.

## 3. Experimental method

### *3.1. Material*

The chosen material, for the experimental validation, is the rate-dependent mild steel DC04 (XES French standards). Its chemical composition is presented in Tab. 2. The quasi-static and dynamic responses of this material are relatively well-known [13, 14, 20, 21] making it a good candidate for method validation. In 2016, Markiewicz *et al.* [26] used a modified Krupkowski model [30] to capture its complex rate-dependent stress flow. The model is inspired from Swift hardening model (or Krupkowski) [36] and from the Hollomon (or Ludwig) model [15] (recovered at the limit of zero strain-rate). It takes the following form:

$$\sigma_{KR} = KX^a \left(\varepsilon_0 X^b + \varepsilon_p\right)^{nX^c}, \text{with} X = \frac{\dot{\varepsilon}_p}{\dot{\varepsilon}_0}, \qquad (21)$$

where $\varepsilon_p$ and $\dot{\varepsilon_p}$ are the plastic strain and strain-rate respectively. Best fit parameters for $K$, $a$, $b$, $c$, $n$, $\varepsilon_0$ and $\dot{\varepsilon}_0$ are provided in Table 3 while Figure 2 presents some results regarding the material tensile response extracted from literature for loading rates ranging from $10^{-3}$ to $10^2$ $\text{s}^{-1}$. The model captures very well the rate-dependent increase of the yield stress as well as the transition from non-linear, steep hardening flow to almost linear perfectly plastic flow at high rate. Notice that presented Krupkowski responses are computed using mean strain-rates (given in legend). The later do not reflects instantaneous strain-rates experienced by the material from 10 $s^{-1}$ which explains part of the discrepancy, the other part being induced by inertial effects (from 200 $s^{-1}$).

### *3.2. Specimen geometry and loading apparatus*

The question of sample design for inverse methods characterization is extremely vast. It can be based on an heuristics approach starting from standardized geometries (see *e.g.* [4, 16]) or using proper optimization approaches, such as *e.g.* constrained topology optimization [2, 6]. In this work, the first approach is used considering flat dog-bone geometry. The main additional features are two symmetrical notches (to avoid loading measurement biases)

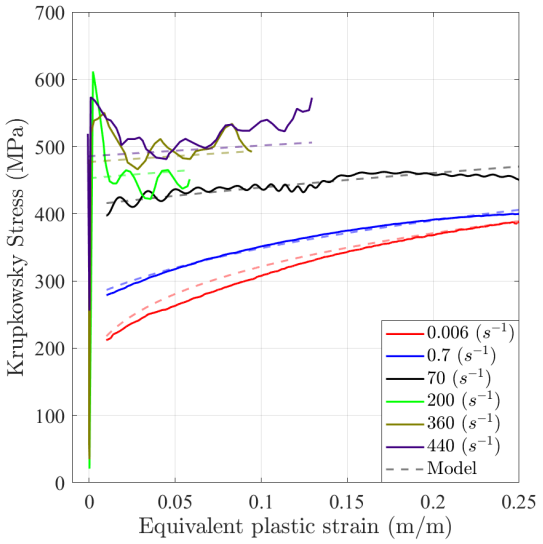


Figure 2: Modified Krupkowski model predictions (see Tab. 3) and tensile reference data reproduced, from [26] (from 0.006 to 70 $\text{s}^{-1}$ using hydraulic test machines) and [14] (from 200 to 440 $\text{s}^{-1}$ using dedicated non direct tensile loading on split Hopkinson bar apparatus).

and a central hole (see Fig. 3a). Such features are expected to lead to strain concentration bands between the notches and the central hole as well as 45° secondary bands pointing down from the central hole to the sample lateral edges. The specimens were cut from a 0.8 mm-thick metal sheet in the rolling direction. The high speed tensile tests is conducted using a hydraulic tensile test machine (MTS-819, 20 kN). The upper grip is mounted on a 2.5 m long 42CD4 steel bar instrumented with strain gauges acting as a Hopkinson bar load cell (see Fig. 3b) to delay inertial biases and to enhance test duration. The lower grip is mounted on a sliding bar and an enclosing case linked to the actuator allowing to reach the imposed displacement speed after a period of "free fall". The selected loading velocity is 5 $\text{m}\,\text{s}^{-1}$ and the associated "free fall" distance was accordingly set to 25 mm.

### *3.3. Imaging setup and DIC parameters*

We use the High spatial Resolution Ultra High Speed (HR-UHS) camera Cordin-580. It is a **multi-sensor**, rotating mirror camera that captures 78 independent images of 8 megapixels (2472 x 3296 pixels) up to 4 million fps. The singularities of the camera, and the numerical developments required to perform quantitative DIC with such a technology have been studied in depth in [39] and will not be recalled in detail here for the sake of conciseness. Nevertheless we strongly recommend, for having a full picture of the metrological consequences coming with this technology to read [39]. Tab. 4 summarizes the main characteristics of the imaging setup. In the present campaign, images are captured at "only"

| C | S | N | Mn | P | Si | Al | Ni | Cr |
|---|---|---|---|---|---|---|---|---|
| 0.0268 | 0.0175 | 0.006 | 0.202 | 0.007 | 0.007 | 0.07 | 0.018 | 0.036 |
| Cu | Mo | Sn | Nb | V | Ti | B | Ca | |
| 0.014 | 0.002 | 0.004 | 0.001 | 0.002 | 0.002 | $\leq 0.0003$ | $\leq 0.0003$ | |

Table 2: XES chemical composition (in wt%) [26].

| $K$ (MPa) | $\varepsilon_0$ | $n$ | $\dot{\varepsilon}_0$ ($s^{-1}$) | $a$ $\times 10^{-1}$ | $b$ | $c$ |
|---|---|---|---|---|---|---|
| 526.6 | 0.024 | 0.221 | 0.085 | 0.002 | 0.385 | 0.002 |

Table 3: Parameters for the modified Krupkowski model from [26].

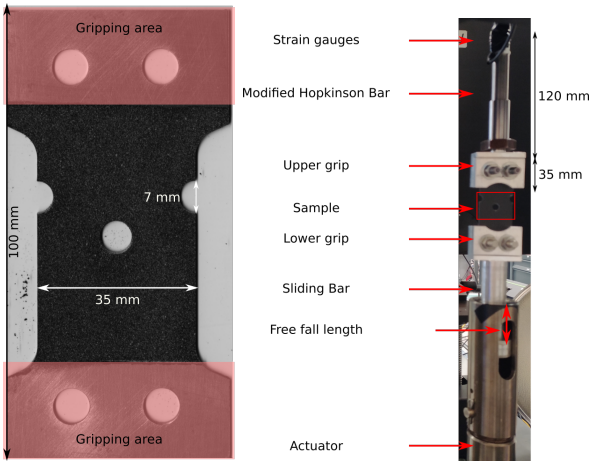


(a) (b)

Figure 3: (a) Sample geometry and (b) Close-up view of the loading apparatus.

68 kfps corresponding to a film duration of about 1.18 ms. The scene is lighted by two Pro-10 Xenon flashes from Profoto (2400 J each in normal mode, at 10 f-stop). In this configuration, the illumination typically lasts 2.4 ms with a stable and optimal plateau of 1.1 ms. The flashes and the camera are triggered separately. Flashes are triggered using an infrared light-gate system (SPX1189 series Honeywell). It is placed in such manner that it sends a 5 V TTL signal when the enclosing case is at a given distance to the contact with the sliding bar. This distance has to take into account the speed of the actuator as well as the rising time of the flashes (150 µs). It has been empirically determined and set to 3.7 mm from the contact point. The Cordin-580 is triggered using the load cell. When the load reaches 6231.5 N, $\approx \frac{3}{4}$ of the plastic yield, a trigger is sent to the camera. Upon receiving the trigger, the camera will record the following images, as well as the ones taken up to 100 µs before (this is named post-triggering). These parameters were determined empirically through preliminary tests. Note that a high speed infrared camera (Telops M3K) is also used to record the other face of the sample during the experiment (see Fig. 4). The infrared results fall out of the scope of the presented work nevertheless, thermal information confirmed that no massive thermomechanical couplings are induced by the strain. Indeed, mean sample temperature rises up to 5 °C while the temperature within localization band does not locally exceed 50 °C at fracture onset. It confirms that the constitutive space used to identify stresses does not have to explicitly take into account temperature (see Sec. 2).

Note that the Hopkinson bar-like load cell implies some adjustments for a perfect time synchronization of the load with images. Indeed, the delay for waves to travel from strain-gauge to image boundary has to be taken into account (see Fig. 3b). Considering, the bar's properties ($E = 205$ GPa and $\rho = 7850\,\mathrm{kg/m^3}$) and a distance of $\approx 155$ mm, the delay is computed as follows: $\tau = \sqrt{\frac{\rho}{E}} = 30\,\mu s$. This is in the order of magnitude of two interframes for this experiment.

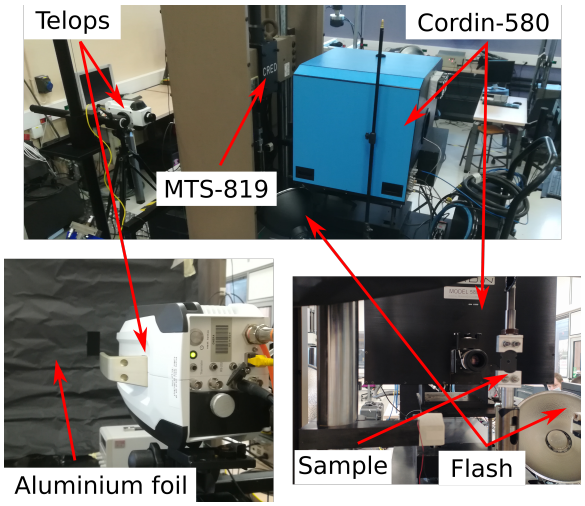


Figure 4: Experimental setup for a high speed tensile test, recorded using a visible-light camera and an infrared one.

Finally, since rotating mirror cameras produce distorted images, an external absolute image reference is needed for performing DIC and for deconvoluting distortions. In this work, this image is obtained by recording, prior to the test, images of the sample at rest with a high definition camera (29 Mpix, Prosilica GT from Stemmer) combined with the same objective lens. The image is eventually down-scaled to the Cordin camera resolution. In addition a series of calibration shots are taken, prior to the test, to create a representative model of the distortions induced by

| | |
|---|---|
| Camera | Cordin-580 |
| Image resolution | 2472 pixels × 3296 pixels |
| Detector Dynamic Range | 12 bits |
| CDS gain<br>*Correlated Double Sampling* | -3 dB |
| CCD gain<br>*analog-to-digital conversion* | +15 % |
| Acquisition Rate | 68 kfps, 15 µs interframe |
| Lens | Tamron 90 mm Macro |
| Aperture | f/2.8 |
| Field of view | 35.8 mm × 47.8 mm |
| Image scale | 1 pixel = 14.49 µm |
| Stand-off distance | 31 cm |
| Patterning Technique | Black and White paint |

Table 4: DIC hardware parameters.

the camera in experimental conditions (lens, working distance, magnification, frame-rate). We use in the following a regularized FE-based DIC strategy [3]. An unstructured mesh refined along expected localization bands and in the vicinity of the notches and the hole is used to parameterize the displacement (see Fig. 1). Tab. 5 summarizes selected DIC parameters for the entire study.

| | |
|---|---|
| DIC Software | Ufreckles [31] |
| Type | FE-based |
| Parametrization | linear FE triangular elements |
| Metric | Zero-Normalized<br>Sum of Squared Differences |
| Pitch | 32 pix (refined down to 26 pix) |
| Regularization | Tikhonov type [41] over 4 × pitch |
| Pre-filtering | image flattening (vignetting) |
| Post-filtering | Savitzky–Golay time filter<br>order = 2, window = 23 frames |

Table 5: DIC analysis parameters. See [39] for uncertainty characterization.

## 4. Metrological assessment using a digital twin

The following section has 3 objectives: (1) numerically find good set of DDI parameters for our case, (2) validate the chosen framework on rate-dependent simulations mimicking experimental loading conditions, (3) produce error bars to better interpret experimental results. Note that, contrary to classical 1D loading cases, the experimental dataset (strain, stress and strain-rate) is multi-dimensional. Hence, for the sake of simplicity the majority of the results will be presented using invariants ($I_1$, $\sqrt{3J_2}$ or Von-Mises). This is not a requirement but just a representation choice, any other norms or invariants could have been chosen.

The digital twin of the experiment relies on both, FE simulations, to produce displacements from a specific structure, boundary conditions, constitutive equation and parameters, and Virtual Image Deformation (VID), to produce realistic images encoding the physics and the experimental biases. They are eventually analysed using DIC, then DDI, as we would do for a real experiment. To be efficient, VID has to take into account: spatial/temporal resolution of the imaging system and the DIC sampling, biases induced by the lens and sensor noise. Obviously such procedure is never perfect, for instance, it is difficult to take into account strong speckle-like pattern transformation or even degradation in highly deformed regions during large strains [40], light variation, out-of-plane motions... Since the procedure has become more and more standard in the validation of an experimental procedure or of inverse identification methods [32, 1, 33, 16, 4, 34, 11, 27, 12], only the main methodological features will be recalled in the following.

### *4.1. Finite Element reference solution and DDI intialization*

All the thermomechanical simulations are performed using the implicit solver of Abaqus. We use CPS3T elements and the phenomenological, multiplicative, isotropic and strain-rate dependent coupled Johnson-Cook model (JC). The yield stress takes the following form:

$$\sigma = \left[A + B\underline{\varepsilon}_p^n\right]\left[1 + C\ ln\left(\frac{\dot{\underline{\varepsilon}}_p}{\dot{\varepsilon}_0}\right)\right]\left[1 - \left(\frac{T - T_0}{T_m - T_0}\right)^m\right], \tag{22}$$

where $A$, $B$, $n$ and $m$ are base material parameters measured below the transition temperature $T_0$. $T_m$ is the melting temperature, $C$ and $\dot{\varepsilon_0}$ define the rate dependence and $\underline{\varepsilon}_p$ is the equivalent plastic strain defined by $\underline{\varepsilon}_p = \int_0^t \sqrt{\left(\frac{2}{3}\dot{\varepsilon}_p : \dot{\varepsilon}_p\right)}dt$. In the following, two sets of material parameters will be used: the **set A** to produce a reference rate-dependent solution (input of the digital twin) and the **set B** which will be use for initializing the DDI procedure. Initializing the DDI can be done with any arbitrary solution but, for the sake of simplicity, we use here the same model but with different parameters. To demonstrate the ability of the introduced DDI framework to capture unknown rate-dependent material responses, the **set B** is, on purpose, chosen having a very weak rate dependence *via* the parameter $C$ and with base parameters $A$, $B$ and $n$ significantly far (up to 50 % difference) from the reference solution obtained with the **set A** . Thermal parameters (useless for the discussion) are kept identical. Tab. 6 summarizes both parameter sets. **Set A** has been identified using data from [26] using quasi-static and $70\,s^{-1}$ loading rates.

From Table 6, we see that the stress solution built from **set B** parameters (*i.e.* for initializing DDI) has a lower yield stress, a stronger non-linear hardening and almost no strain-rate dependence. The question addressed in this part is the ability of the proposed DDI framework to recover the reference solution (**set A**) starting from an ar-

| set | $A$ (MPa) | $B$ | $n$ | $C$ $\times 10^{-4}$ | $\dot{\varepsilon}_0$ ($s^{-1}$) | $m$ | $T_0$ (K) | $T_m$ |
|---|---|---|---|---|---|---|---|---|
| **A** | 394 | 136 | 0.47 | 256 | 70 | 1.1 | 300 | 1350 |
| **B** | 315 | 272 | 0.61 | 2.56 | | | | |

Table 6: Johnson-Cook model parameters: **set A** is for reference solution and **set B** for DDI method initialization.

bitrary one which does not encode the right constitutive features. To facilitate field comparison, simulations are performed using the actual experimental DIC mesh (see Fig. 1). The same mesh will be used throughout the whole procedure. Also, the analysed simulation time steps are chosen to match the experimental frame-rate. With respect to boundary conditions and simulation outputs, two cases must be distinguished:

- the reference solution is produced (using **set A** parameters, see Tab. 6) imposing, at the lower boundary (see Fig. 1), an axial displacement corresponding to a constant velocity of $5\,\mathrm{m\,s^{-1}}$ while maintaining the upper boundary clamped. The outputs of this simulation – namely the displacement fields $U^{\mathrm{ref}}$, the stress fields $\boldsymbol{\sigma}^{\mathrm{ref}}$ and the vertical net force on the upper boundary $F_y^{\mathrm{ref}}$ – will serve as references for virtually deforming images (and perform DIC) then evaluating performances of the DDI method.
- the DDI initialization is produced (using **set B** parameters, see Tab. 6) in two steps: first, a simulation is ran with DIC displacements (obtained from VID using the reference solution) imposed at the mesh boundaries. The resulting load distribution on the upper boundary is rescaled to match the net force of the reference simulation ($F_y^{\mathrm{ref}}$) and stored. Then, another simulation is ran with mixed boundary conditions, replacing the upper axial displacement by the saved axial load distribution. This rather complex strategy allows imposing a realistic load distribution in the simulation knowing only displacement and net force like in a real experiment. The main output of this simulation is the stress field, $\boldsymbol{\sigma}^{\mathrm{false}}$ balancing the reference net force $F_y^{\mathrm{ref}}$, used then for initializing DDI. The upper script *false* underlines that it is far from the sought target $\boldsymbol{\sigma}^{\mathrm{ref}}$ evenif it balances the external net force.

### *4.2. Focus on Virtual Image Deformation*

This part gives the main ingredients of the VID. While the global procedure is standard some extra steps come when trying to mimic our particular camera. A real image of a speckle-like pattern is synthetically deformed using $U^{\mathrm{ref}}$. To account for Cordin-580 optical distortions (see [39]), $U^{\mathrm{ref}}$ is composed with distortion fields $U^{d_1}$, calibrated experimentally. The composition equation takes the following form:

$$U^{\mathrm{virtual}}(\underline{X}) = U^{\mathrm{ref}}(\underline{X}) + U^{d_1}(\underline{X} + U^{\mathrm{ref}}(\underline{X})). \qquad (23)$$

Where $U^{\mathrm{virtual}}$ is the displacement imposed to the images and $\underline{X}$ are the coordinates. In practice, filling the deformed image with the right grey level values at integer pixel positions requires to get the inverse mapping of the transformation and a grey level interpolation scheme. We use in the following a bi-cubic spline interpolation. Finally, a realistic noise is added to the deformed and distorted synthetic images. Apparent sensors noise is obtained by computing, over a real image sequence of a sample at rest, the temporal standard deviation of material point grey level values (it implies correcting distortions first, see [39]). Figure 5 shows the Cordin-580 apparent noise (normalized by the dynamic) as a function of the grey level intensity and pixel density. We see that it is signal-dependent (or heteroscedastic) which follows a non-linear trend from 30 % in dark areas down to 5 % in bright ones. Hence, we corrupt synthetic images adding a zero-mean random noise whose the standard deviation depends on the grey level according to the polynomial fit shown on Figure 5. As a side comment, note that data presented in Figure 5 is not strictly speaking a sensor noise. Indeed, it also results from the offset and gain mismatch from one sensor to another (multi-sensor technology), the focus mismatch, as well as the uncertainty on distortion estimation which does not allow for perfectly stabilizing images ($\pm$ 0.1 pixel). This is why we name it apparent noise. In addition, it explains why values are very high compared to mono-sensor ultra-high speed camera (*e.g.* in the order of 1 % of 16 bits for the Shimadzu HPV-X). It is the price to pay for having 8 Mpix images (up to 4 Mfps) compared to 0.1 Mpix for a Shimadzu HPV-X at same frame-rate.

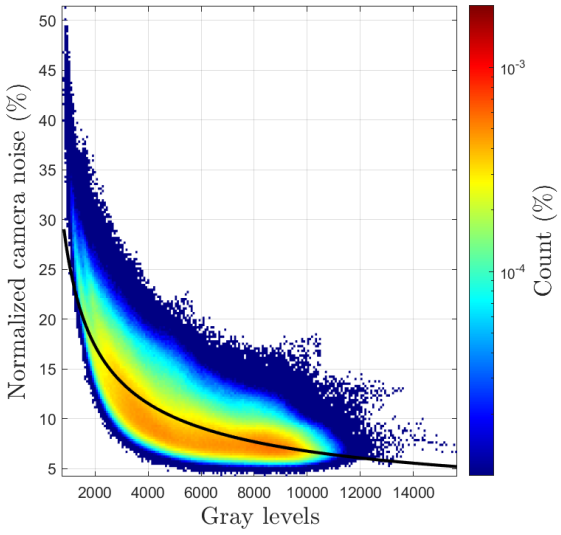


Figure 5: Normalized apparent camera noise (in %) *versus* the mean grey level. The colour denotes the pixel counts (in %), while the black line denotes the polynomials used to model the camera noise.

Eventually, the DIC procedure proposed in [39] is

applied on these synthetic images and displacement fields can be used as an input for DDI. Notice that a small trick is required here to accurately mimic the experimental variability of optical distortions from one shot to another, hence the fact that optical distortions are only known (from calibration) with a certain level of confidence. It consists in using an other set of optical distortion field $U^{d_2}$ when deconvoluting, within the DIC, actual displacement from distortions. In practice, variability of optical distortion modes from one shot to another is statistically evaluated experimentally, hence $U^{d_2}$ is defined as $U^{d_1}$ plus or minus such a variability.

The whole digital twin procedure is summarized in the Figure 6. Later-on, the exact same procedure will be used for analysing the experiment without the upper left brick *creation of a numerical twin* for which only $U^{\text{DIC}}$ and $F^{\text{ref}}$ will be known. With all these ingredients, the experimental process is mimicked with a high degree of confidence. Displacements coming from DIC encode the response of a known rate-dependent model and are corrupted by main experimental biases (sensor resolutions, noise, variability of optical distortion, speckle-like pattern quality, DIC algorithm convergence). The initialization of the DDI balances actual external forces but is selected far enough from the sought solution. Identified stresses, $\sigma^{DDI}$, can be quantitatively compared with $\sigma^{\text{ref}}$ on the same mesh.

### *4.3. Numerical results and discussion*

The stress identification is performed on 50 simulation time steps (leading to $\approx 40\,\%$ local peak strain). First the influence of the different parameters (see Tab. 1) of the DDI will be investigated. Then, once the parameters chosen, the DDI method performance will be discussed.

***Influence of the DDI user parameters.*** To investigate the influence of the different parameters of the method, several Data-Driven Identifications were performed on the same simulation. Different numbers of material states $N^*$ are tested such that: $30 \leq \frac{(N_t-1)\cdot N_e}{N^*} \leq 200$. The ratio between the pseudo elastic modulus and the actual material Young Modulus, $\frac{E_o}{E}$, is swept from 0.1 to 10. Finally two forms of the weighting matrix $[p]$ are tested, either $\mathbf{I}_2$ or $[w]$ (see Sec. 2.5). In addition a median filter ranging from 0 to 5 neighbouring elements (noted $l_c$) is applied to DIC strains before the DDI to see if any pre-filtering of the noisy experimental strains is required for optimizing performances of the identification. In order to assess which quadruplet leads to the best identification results, the following equivalent standard deviation $\xi_{\text{eq}}$ is considered:

$$\begin{cases} \xi_{\text{eq}}(\underline{\underline{\sigma}}_{\text{DDI}}) = & \left(\frac{1}{3}\sum_i \mathcal{V}ar\left(\Delta\sigma^i\right)\right)^{\frac{1}{2}}, \\ \Delta\sigma^i(e,t) = & \sigma^i_{\text{DDI}}(e,t) - \sigma^i_{\text{ref}}(e,t) \end{cases} \tag{24}$$

where $e$ is the element (single quadrature point), $t$ is the time, $\mathcal{V}ar$ is the variance, and $i$ is the in-plane tensor component $xx$, $yy$ and $xy$ respectively. Thus, the error is the square root of the variance of the difference between the identified stresses and the reference ones for all the elements and time steps, averaged over the three components.

| $N^*$ | $E_o$ | $l_c$ | $[p]$ |
|---|---|---|---|
| $\frac{1}{30}(N_t-1)\cdot N_e$ | $10\times E$ | 2 | $[w]$ |

Table 7: Optimized DDI user parameters.

The best parameters among those tested are given in Table 7. Figure 7 depicts the evolution of $\xi_{\text{eq}}$ when 3 out of 4 parameters are fixed and one varies. This figure shows that the error increases when the number of material states decreases. Furthermore, the error decreases when $E_o$ increases. These trends are in line with the observations from [8]. In addition, this figure highlights that there is an optimal filtering length for DIC strains: $l_c = 2$. At last, the choice of the weighting matrix do not have a significant influence on the error. Nevertheless, the use of $[w]$ leads to a small reduction of the error (from 24.8 MPa to 23.7 MPa). As a summary, a stress identification error of about 20 MPa is expected on average over the test, when considering our particular camera, geometry, loading case scenario and a Johnson-Cook rate-dependent based material. In the rest of document, DDI user parameters presented in Table 7 will be used.

***DDI Post-processing.*** Let us now visualize the identified material response, looking at the identified mechanical states distribution in a Von-Mises $\{||\varepsilon||_{VM}, ||\sigma||_{VM}\}$ space. Figure 8a shows all identified mechanical states for all time steps during the simulation in this Von-Mises space. The count shows how the test samples (densely or not) the constitutive space. Firstly, it is logical that the mechanical response appears "thick" in this space. Indeed, simulations are rate-dependent and strain-rate fields are heterogeneous due to notches and hole. So part of the spread is due strain-rate dependence whose the dimension is not represented. This is one of the asset of heterogeneous tests; testing various strain-rates at a time. Nevertheless, the spread in Figure 8a is clearly dominated by the experimental biases introduced in the VID procedure. Indeed, a main response is clearly observed (characterized by mechanical states with high occurrence numbers) surrounded by a massive spread. This spread is especially significant for strains beyond $0.4\,\text{m}\,\text{m}^{-1}$ as it reaches more than 150 MPa. Nevertheless, the occurrence of the mechanical states in the spread are several order of magnitude below the occurrence in the main response. Since the DDI method is based on clustering, it stands for a reason that the most recurrent mechanical states will lead to more robust identification. Hence robustness is strongly dependent on the density distribution of the mechanical states in the constitutive space: database outliers, *e.g.* extreme localization (in space or time) can not be properly handled.

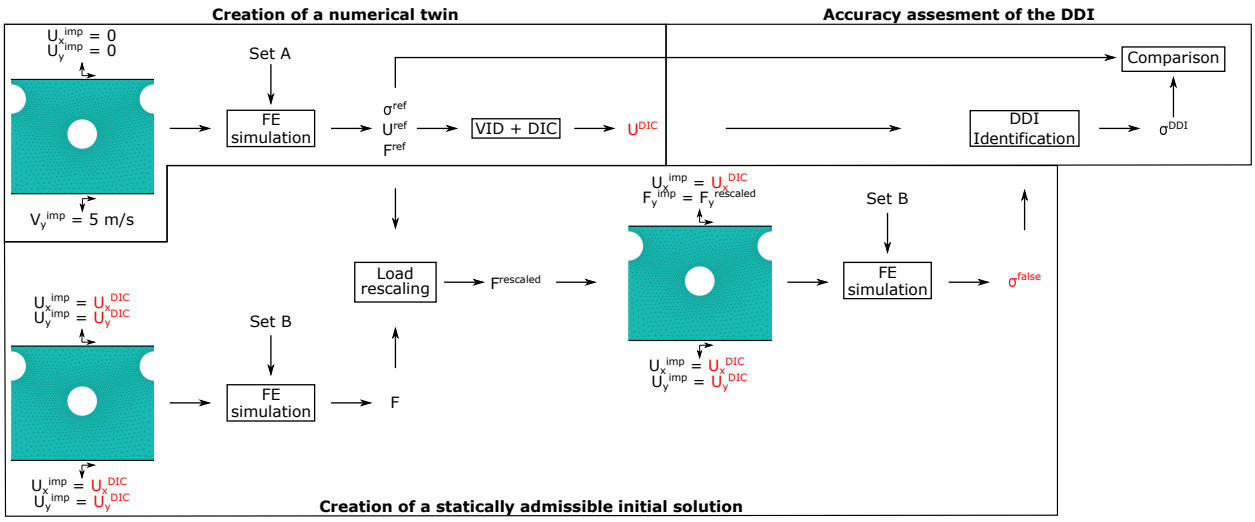


Figure 6: Schematic of the numerical test case procedure. In red are the inputs of the DDI algorithm.

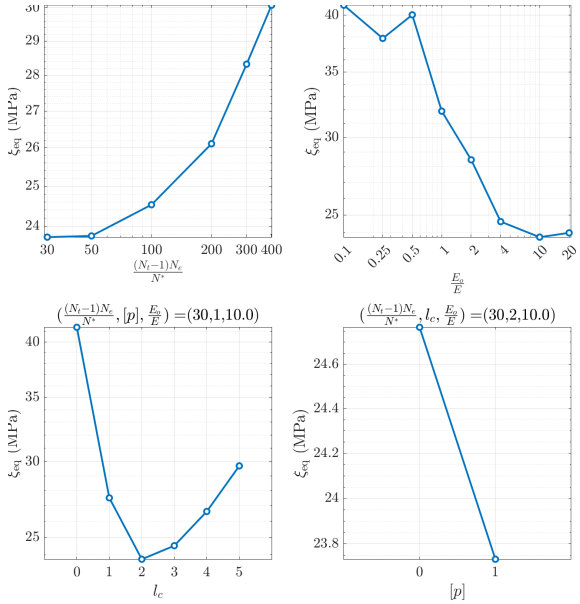

Figure 7: Evolution of $\xi_{\text{eq}}$ with respect to the DDI parameters. Note that the y-scale differs from one graph to another.

In that context, the definition of a DDI post-processing, filtering states according to their occurrence seems relevant. In what follows, a mechanical states is considered relevant if its occurrence is higher than the $95^{\text{th}}$ quantile. Figure 8b shows the mechanical states remaining after the proposed filtering. As expected, only the main response is kept and the mechanical states spread is significantly reduced. Notice, that when using this filtering, only 9 % of the whole set of mechanical states (space and time) is discarded. This supports the use of this simple (not case dependent) filter since it improves significantly the interpretability of the DDI results while discarding a minimal amount of data. Figure 8c spatially spots for how many time-steps the local states have been discarded, expressed in percentage. Indeed, the robustness of an identified state can vary over time since a spatial area can shift from a densely sampled region, in the constitutive space, to a weakly dense or the other way around. This figure shows that most of the elements are kept for all time steps. Also, the elements discarded are located near the notches and the central hole probably at the end of the test when they are subjected to extreme and rare (in the database) loading conditions. In the rest of this document, all the results will be presented post-processed as such, *i.e.* discarding outliers.

***Local stress assessment.*** Considering optimized DDI user parameters and its post-processing, expected errorbars on local stress measurement can be established. It seems irrelevant to only provide a global scalar value for an heterogeneous test, hence we propose a more thorough investigation looking at the systematic link between, stress identification error, local stress level and stress occurrence in the database.

Figure 9 presents the stress identification uncertainty (that is to say the standard deviation of $\Delta\sigma^i(e,t)$) achieved for a given local stress magnitude. The figure shows the absolute uncertainty in red and relative to the local stress magnitude in blue. On top the distribution presents how much each class of stress magnitude is sampled by the test. The distribution indicates that a significant amount of material points (space and time) are subjected to stress magnitudes below 100 MPa. This corresponds to the very first part of the elastic domain of the considered material (see Fig. 8b). Relative uncertainty is the highest in this region, from 100 % for low strains down to 11 % at 100 MPa. It evidences that the signal to noise ratio is there not favorable for identification. This is the direct consequence of the strain uncertainty (2 $m\varepsilon$, see [39]) induced by our

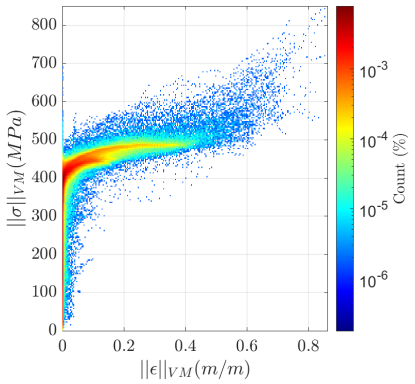


(a) Raw mechanical states,

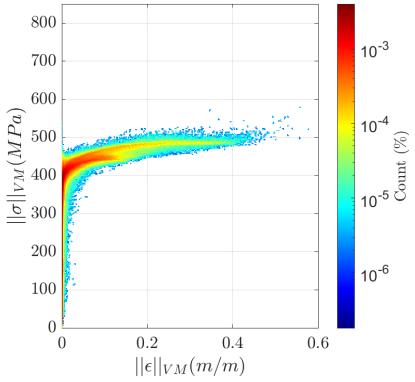


(b) Post-processed mechanical states,

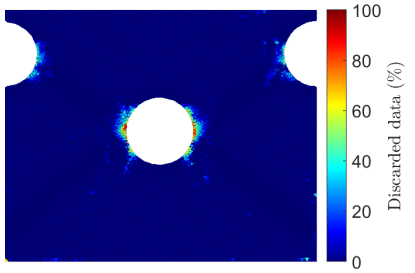


(c) Spatial localization of discarded states,

Figure 8: Mechanical states distribution in the $\{||\varepsilon||_{VM}, ||\sigma||_{VM}\}$ space before and after DDI post-processing. In Fig. 8c, 0 % means that the local data are kept whatever the loading stage while a higher value means that they are discarded for some. 100 % means fully discarded.

camera and not the DDI method itself. Then we observe that few data are available during the elasto-plastic transition, *i.e.* in the 200 MPa – 400 MPa range. The consequence of such a data scarcity is visible on the absolute stress uncertainty. Indeed, as the data availability in this range decreases, the absolute stress uncertainty increases from 9 MPa at the beginning to 27 MPa for a stress level of 315 MPa. Nevertheless, since the signal to noise ratio becomes favorable, the relative stress error remains below 10 % beyong stress magnitudes of 200 MPa. At last, more data is available beyond 400 MPa *i.e.* during plasticity. The figure shows that beyond this stress magnitude, the error remains below 16 MPa *i.e.* a relative error below 4 %. Notice that such results are camera, geometry and loading dependent and should be checked for every new configuration.

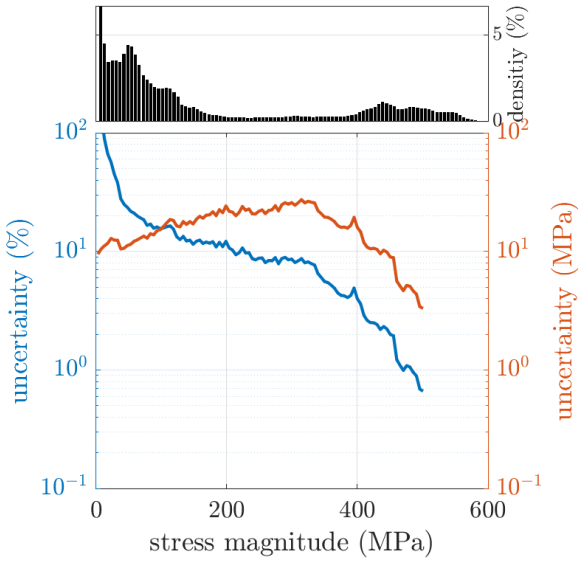


Figure 9: Stress uncertainty with respect to the stress magnitude. The stress magnitude occurrence in the test is given by the histogram while the blue and red lines are respectively the relative and absolute values of the stress uncertainty. The values are obtained after DDI post-treatment

***Range of local loading scenarios.*** DDI allows for probing local mechanical response giving the unique opportunity to analyze richer tests without assuming a constitutive equation. Let us check if the loading configuration and geometry, presented here, allow for probing various multiaxial responses in a single test, and how DDI performs in each of them. Figures 10a and 10b respectively depict the distribution of the mechanical states and their associated identification errors, this time, in the $\{I_1, \sqrt{3J_2}\}$ space. Indeed this space can be used to assess the triaxiality level reached by each material point at every time during the experiment. The distribution shows that despite the introduction of a central hole and notches, most of the reached mechanical states are close to uniaxial tension with a slight tendency to spread toward pure-shear or equi-biaxial tension in plastic regime (beyond 394 MPa). Some uniaxial compression states are reached, but in elastic regime where the signal to noise ratio is not favorable. It is confirmed looking at 10b where we observe again that below 200 MPa the identification error

is massive whatever the triaxiality level and remain higher than 20 % for all points undergoing uniaxial compression. Furthermore, this figure shows that the identification error is lower for higher stress magnitudes (as already evidenced Fig. 9) but more importantly that these states are mainly under uniaxial tension. These observations are important since they evidence that whatever the complexity of the geometry, at least with such an heuristic design, multiaxiality and non-proportional loading would only be densely introduced within the sample using additional actuators. In the present case, it could be shown that local principal stress directions significantly varies, *i.e.* useful for characterizing anisotropy, nevertheless multiaxiality is mainly reached either by some outliers, close to boundaries, or for very small strains, close to noise floor. Sample design optimization for DDI achievement should take all these points into consideration.

At last, let us check the ability of the DDI method to retrieve the strain-rate dependence of the reference solution. For this purpose averaged stress-strain curves, for mechanical points undergoing similar mean strain-rates during the loading are computed. Firstly, the average strain-rate over time for each element is computed. Then, they are clustered in 20 mean strain-rate groups (using K-means algorithm). Finally, independent stress-strain curves are computed by averaging stresses and strains for each group. Figure 11 shows the relative errors, between identification and reference solution, as a function of the strain-rates. The dashed lines depict the initialization error (simulation using parameter **set B**), while the stars depict the DDI converged solution. This figure confirms that during the convergence of the DDI, stress fields shift from about 10 % error (initialization) down to 5 %. Furthermore, this figure evidences that the framework is able to retrieve the underlying strain-rate dependence evenif if the initial stress solution did not include it. This is supported by the fact that the relative error remains nearly constant below 6 % while it was linearly increasing initially. In short, evenif the initialization does not truly capture the physics, DDI makes the features of the constitutive model, hidden within strain fields and load through equilibrium, naturally appear.

To summarize, considering optimized DDI user parameters given in Table 7, a DDI post-processing consisting in discarded the 5 % lessest occurring mechanical states, our sample geometry, loading conditions and camera, the conclusions are:

- Below 100 MPa the signal to ratio is not favourable, due to the noise on the strain measurements. The related mechanical states are undergoing elastic strains and are mainly located above and below the hole and notches.
- Since the propose method is based on clustering, the abundance of similar data leads to lower stress identification errors. Indeed, when data is sufficiently abundant errors remain below 5 %. This is mainly the case here in plastic and uniaxial loading regime.
- From a general point-of-view stress identification error lower than 10 % are expected for stresses higher than 200 MPa, *i.e.* half of the elastic regime.
- In the considered experiment most of the mechanical points are subjected to uniaxial tension, despite the holed and notched geometry.
- At last, the differential DDI framework is able to retrieve the global strain-rate dependence of the material within 6 % of error. It proves that the chosen

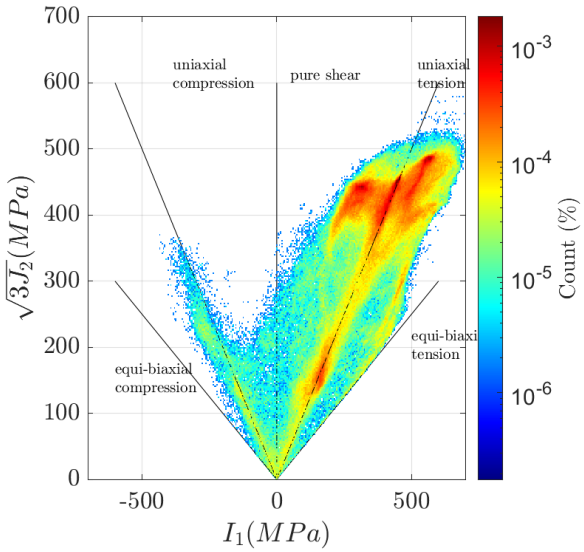


(a) Mechanical states distribution,

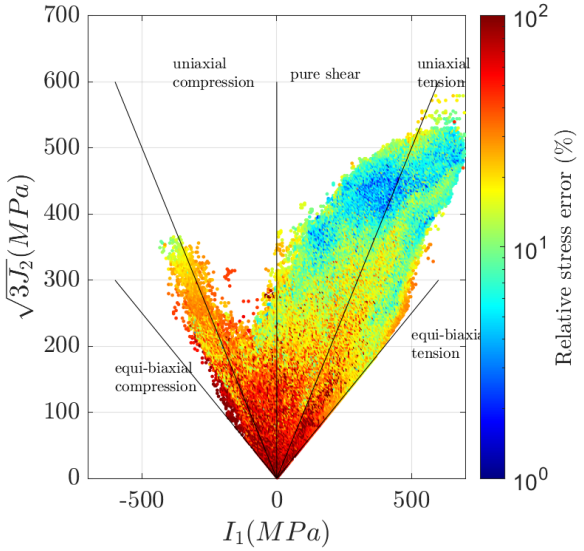


(b) Relative stress identification error,

Figure 10: Mechanical states and errors in the $\{I_1, ||\sigma||_{VM}\}$ space.

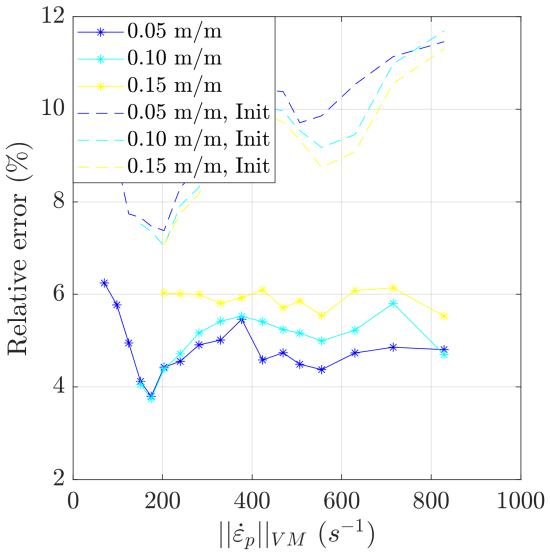


Figure 11: Relative stress identification error evolution with respect to the strain-rate. The stars represent the converged DDI solution while the dashed lines refer to the DDI initialization using **set B** parameters.

DDI framework can capture, at least for monotonic loading, such a material hidden feature.

## 5. Experimental application

This section finally analyses the tensorial database $(\underline{\varepsilon}, \underline{\dot{\varepsilon}}, \underline{\sigma})$ produced during the heterogeneous, dynamic and uniaxial test discussed in previous sections. First, variation of macroscopic quantities are discussed, then kinematic fields. Eventually, identified stress fields are analysed and the rate-dependence of the material discussed in relation with predictions of the modified Krupkowski model. To clarify the deformation scenario, figure 12 shows firstly the last image (distortion-free) obtained during the high speed tensile test. In this image two cracks can be seen. On the left hand side, there is a crack going from the central hole to the notch. On the right hand side, the crack only started to initiate from the central hole. In what follows, the analysis is performed on the images prior to the apparition of these cracks.

### *5.1. Mean trends*

Figure 13 depicts the evolution of different quantities of interest during the experiment. The three vertical dashed lines are the time steps for which associated fields will be discussed later-on. Note that the zero in the timeline corresponds to the time when the Cordin-580 is triggered by the load cell. Figure 13a plots the evolution of the Von-Mises norm of both the strain (in blue) and strain-rates (in red) on average in the left localization band during the experiment (see Fig. 12). This figure shows that during the first 100 µs of the experiment, the material is mainly

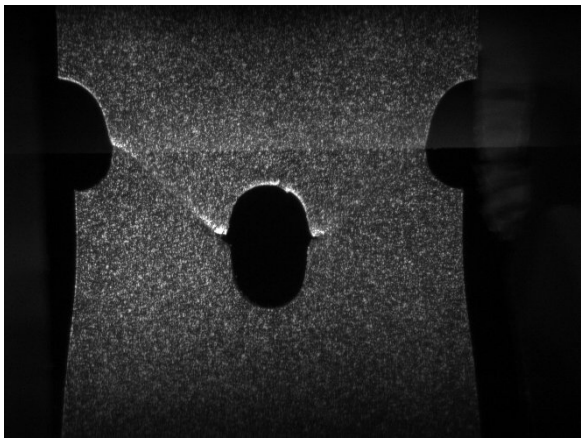

Figure 12: Last image (distortion-free) of the sample obtained during the test.

in an elastic regime ($||\varepsilon||_{VM} \leq 0.005$). The strain in the localization band is higher than 0.01 after about 150 µs, then increases following a ramp up to 0.22 at the fracture onset. Two stages are observed in the strain-rate evolution. First, it ramps up to 375 $s^{-1}$ in about 300 µs. Then, it reaches a plateau and oscillates between 350 $s^{-1}$ and 400 $s^{-1}$. At last, Figure 13b shows the evolution of the load during the experiment (in blue). It also depicts – for information purpose only – the average temperature increase (in red) in the considered band. Two stages can be evidenced for the load. During the first 150 µs the load ramps up until 8 kN. Then it reaches a plateau and oscillates around 8.5 kN. Considering an initial cross section $S_0$ equal to $1.68 \times 10^{-5}$ $m^2$ (subtracting the holes), the engineering stress can be estimated at 500 MPa. This value is in line with the ones obtained in [14].

### *5.2. Kinematic fields*

Figure 14 shows distortion-free sample images, axial displacement and Von-Mises strain fields (both from DIC) and identified Von-Mises stress fields (from DDI) for the three time steps introduced previously. The displacement fields obtained are consistent with a tensile test. The first two images underline the fact that the tensile test is not perfectly uniaxial. Indeed, the axial displacements are higher on the left-hand side of the sample. In turn, crack initiates on the left-hand side of the sample before the right-hand side. It as been systematically observed for multiple experiments. It may be due to a slight misalignment / deformation of the holding rods. The sample geometry induces primary and secondary localization bands as predicted by the FE simulations with little strain everywhere else. While it is 0.2 on average within the localization bands it reaches more than 40 % at the hole borders where cracks eventually start. Regarding strain-rates, not presented here (similar to strain fields), it varies between 10 and 400 $s^{-1}$ with the majority of the values below 200 $s^{-1}$. Nevertheless it is important to notice that

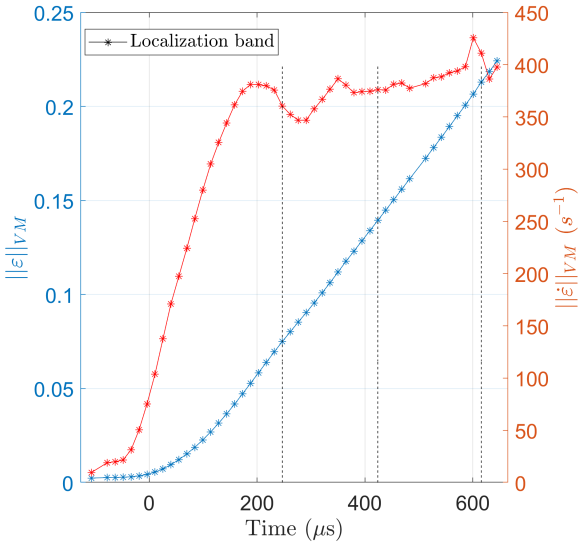


(a) Mean Von-Mises strains and strain-rates,

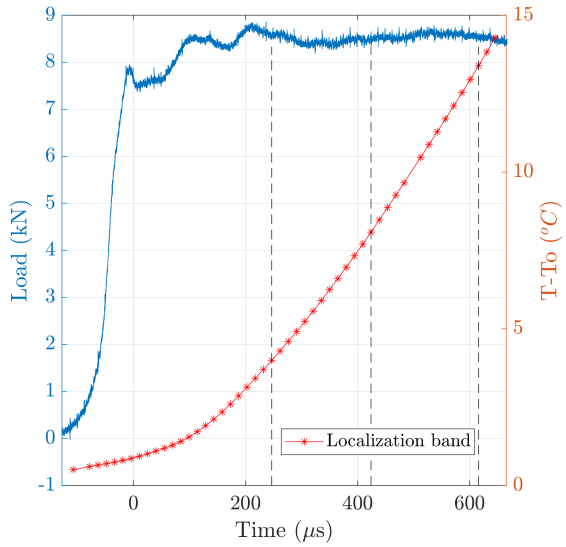


(b) Load and mean temperature,

Figure 13: Evolution of different quantities of interest during the test. Except for the load, all quantity are averaged within the left localization band (see Fig. 12) to underline peak values.

strain and strain-rates are not independent, high strain-rates values are only reached by heavily strained regions and the other way around.

### *5.3. Mechanical response*

Stress fields (shown in Fig. 14j) are obtained using a procedure similar to the one presented in Fig. 6, but in this case the reference solution and the underlying model are unknown. $F_y^{\text{ref}}$ is measured by the load cell, $U^{\text{DIC}}$ is computed using the experimental images and DIC, and the DDI initialization $\sigma^{\text{false}}$ is computed using the two steps procedure and a JC model with **set A** parameters (see Tab. 6). Let us recall that a classical multiplicative Johnson-Cook model, even with **set A** parameters (coming from [26]), cannot capture the complex strain-rate dependence of the XES material contrary to the Krupkowski model, specifically designed for it. In particular, JC model fails to describe the uncoupled dependencies of the initial yield stress and the hardening modulus (see [38] for parametric study). In that sense, like in the numerical section, the DDI initialization is significantly far from the sought solution. The DDI parameters are the one presented in Tab. 7 and the DDI post-processing strategy introduced in Sec. 4.3 is used.

***Stress fields.*** Von-Mises stresses fields (Fig. 14j), as expected, show that the notches and the central hole create plastic strains concentration bands. In these bands the Von-Mises stresses reach eventually about 500 MPa. In addition, in the secondary bands (*i.e.* pointing down), the stress is about 400 MPa. Above and below the central hole and the notches the stress magnitudes remain below 200 MPa. These observations are consistent with the numerical study performed. Let us remind that a large part of the field is expected to be identified with high confidence (5 % error beyond 350 MPa), intermediate stresses are expected to come with 10 % error (from 200 to 350 MPa) while lower stress values come with a higher level of uncertainty, especially dark blue regions (below 100 MPa) (see Fig. 9). A puzzling results is the decrease of the stress amplitude, in the localization bands. Indeed, at 247 µs the stress goes beyond 500 MPa, while it falls down to 450 MPa at 616 µs, although the three analyzed states are located in the macroscopic plastic plateau (see Fig. 13b). It may be resulting from a softening behavior beyond a certain level of strain-rate. Again, temperature is not expected to play any role here since it does increase by more than 15$^o$C on average in the bands.

Figure 15 presents stress, strain and strain-rate distributions in $(I_1, \sqrt{3J_2})$ and $(\|\varepsilon\|_{VM}, \|\dot{\varepsilon}\|_{VM})$ spaces respectively, during the experiment. The loading paths of a few selected elements, spotted in 15c, are superimposed on these distributions. Notice that mechanical states are colored according the local density of datapoints (see colorbar) and additional colors are used to point the selected 5 different loading histories. Figure 15a shows, as expected, that the sample is mainly under uniaxial tension but with slight variation of triaxiality depending on the spatial region of interest (*e.g.* primary or secondary localization band). Some compression and shear states are reached within the specimen mainly on top or below the hole. Looking at a particular loading path (the yellow one for example) we also see that the loading history is proportional, having in mind that all states start at zero. In addition, Figure 15b shows that the strain and strain-rate mean spectra underwent by the specimen are $[0 - 0.18]$ and $[0\,\text{s}^{-1} - 450\,\text{s}^{-1}]$. The figure clearly highlights that

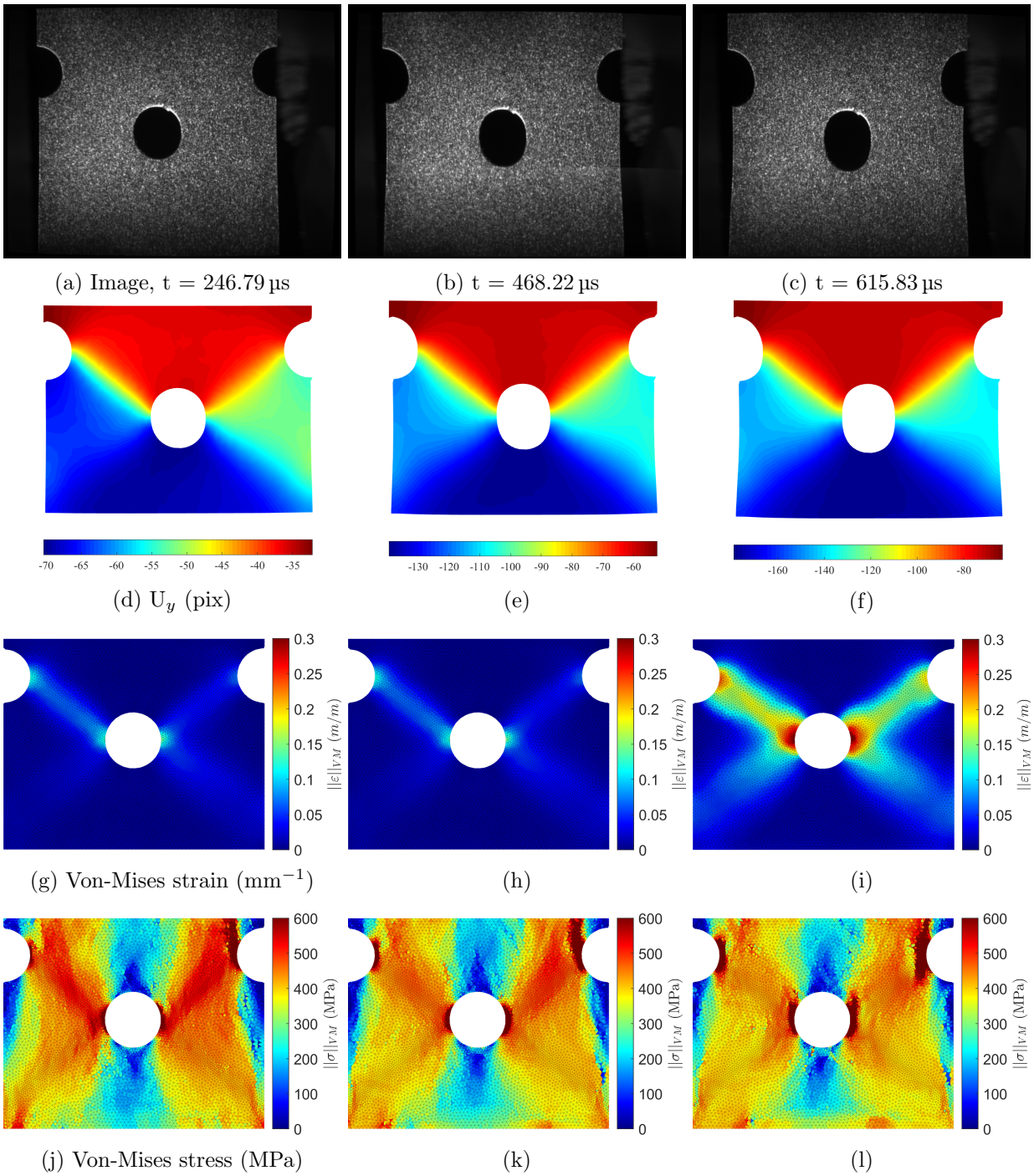


Figure 14: Distortion-free images (from a to c), axial displacement fields (from d to f), Von-Mises strain fields (from g to i) and Von-Mises stress fields (from j to l), extracted at 246.79, 468.22 and 615.83 $\mu s$ during the dynamic tensile test.

the different regions of the bands are under different but quasi-constant strain-rates, at least during plastic regime. Nevertheless, this figure emphasizes a complexity inherent to all dynamic tests (even statistically determinate ones): material points in the elastic regime, in the elasto-plastic transition, then in stabilized plastic regime do not necessarily undergo same strain-rates. Analysing a dynamic test from a mono-parametric point of view, *i.e.* considering an average strain-rate may be inaccurate since Young-modulus, yield-stress and flow hardening are actually not submitted to similar rate conditions. Notice that we will nevertheless consider in the next part averaged strain-rates over the test to observe the global rate-dependent response of the material. Again, this is not a requirement of the DDI method, but a simple post-treatment of the built database for visualization / interpretation purpose. We

also observe a singular response at the fracture initiation location (green path on the figure). Instead of stabilizing, strain-rate level significantly drops after reaching a peak at 600 $s^{-1}$. The reason of such a behavior is not clear especially considering that the crack did not start yet, at least visually.

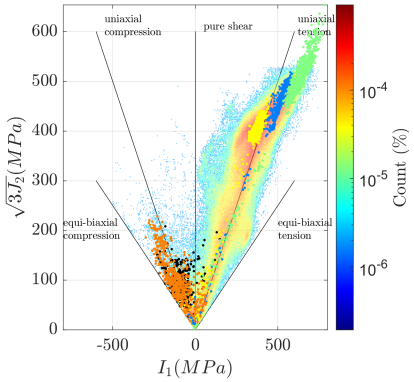


(a) Stress states distribution,

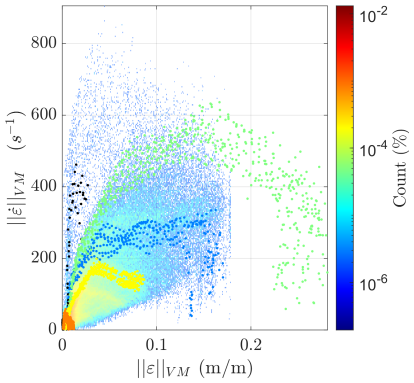


(b) Strain and strain-rate distributions,

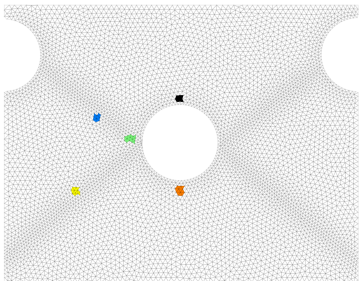

(c) Location of spotted elements,

Figure 15: Stress, strain and strain-rate distributions in ($I_1$, $\sqrt{3J_2}$) and ($\|\varepsilon\|_{VM}$, $\|\dot{\varepsilon}\|_{VM}$) spaces respectively, during the experiment. The loading paths of a few selected elements, presented in *c*, are superimposed on these distributions (see colors).

***Rate-dependence characterization.*** As introduced in Sec. 4.3, the strains, strain-rates and stresses data can be used to discover the rate-dependence of the material. Several iso-strain-rate responses are computed from the dataset by averaging strain and stress values of mechanical points undergoing similar mean strain-rates over the test. It allows reducing noise through an averaging process but also presenting strain-rate dependence of the material in a simple 2D ($\|\boldsymbol{\varepsilon}\|_{VM}$, $\|\boldsymbol{\sigma}\|_{VM}$) space. Again, such representation may be questionable since according to figure 15b material points does not necessarily undergo constant strain-rates over the test duration (as for any dynamic test), especially beyond 200 $s^{-1}$. It is nevertheless the only way to produce full elasto-plastic iso-strain-rate curves. Indeed, high strain-rates levels are only reached for large strains and the other way around, hence considering instantaneous strain-rate instead of test average would only allow to represent small portions of the response for a given strain-rate.

Ten iso-strain-rate XES responses have been *a posteriori* reconstructed and are plotted on Figure 16a. Selected mean strain-rates range from 17 $s^{-1}$ to 266 $s^{-1}$ with steps of approximately 25 $s^{-1}$. While the test reaches higher strain-rates, high strain-rates regions are only sampled by few points, as a consequence, they disappear in the following clustering. In short, data at 266 $s^{-1}$ includes in its average, few points undergoing higher strain-rates. As previously discussed, strain and strain-rate amplitudes are related. Hence the higher is the strain-rate, the higher is the strain amplitude. It explains why high iso-strain-rate curves show more of the plastic regime compared to low iso-strain-rate curves. In the present case, below 50 $s^{-1}$ the plastic yield is not even reached. In this context, the ending of each curve should not be interpreted as a fracture limit but only as the maximum strain undergone by each iso-strain-rate set of mechanical points within the test. Only the higher strain-rate curve (localization band response in orange in Fig. 16a) reaches the fracture onset. Some points can be underlined. The material is rate-dependent. Apparent yield stress range from 380 MPa to 450 MPa when the strain-rate varies from 50 to 188 $s^{-1}$. A non-linearity appears about the same stress value for higher strain-rates but peak stresses continue to increase. This rate-dependence seems to fade-off beyond 200 $s^{-1}$. This is in line with literature results presented in Fig. 2. Up to 188 $s^{-1}$, the material response is almost perfectly plastic with a slight tendency for the hardening modulus to decrease when increasing the strain-rate. Contrary to Fig. 2 at 200, 360 and 440 $s^{-1}$, no overshoot is observed in the early plastic regime. While in the literature data are obtained using a modified split Hopkinson bar apparatus, probably in the inertial regime, where data can be corrupted, this is not the case for our experiment where, thanks to a modified loading setup (see Sec. 3.2), inertial waves come back into the sample only after 1.1 ms (*i.e.* about the fracture onset). High strain-rate responses do not oscillate compared to literature (see Fig. 2) which completes our previous argument. We use here an hy-

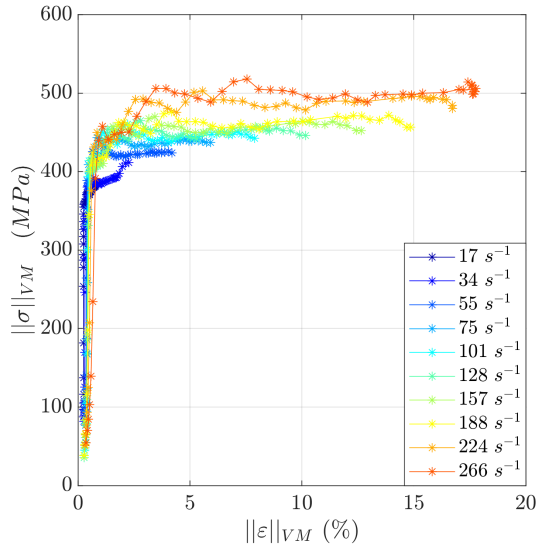


(a) Iso-strain-rate stress-strain curves reconstructed from the experimental database,

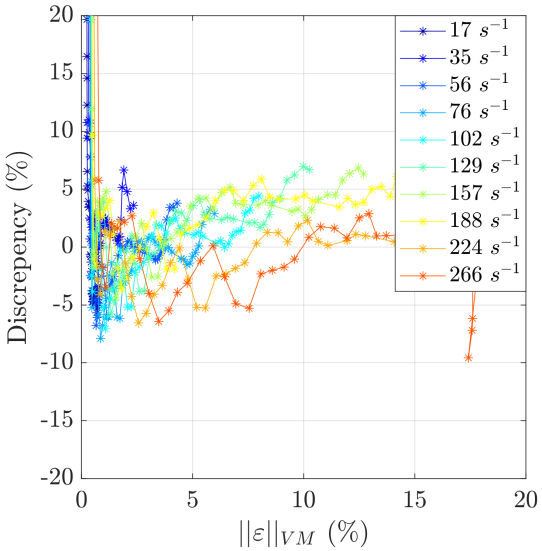


(b) Discrepancy between DDI results and modified Krupkowski prediction using parameters 3,

Figure 16: Strain-rate dependence of the XES steel and deviation from model prediction.

draulic tensile test machine with holed sample to capture strain-rates usually reached with impact tests, where inertial effects can have huge consequences on measurements robustness. Finally, the softening behavior observed on the stress fields, especially in the localization band, is not really visible anymore after such an iso-strain-rate averaging process. Averaging the local stress-strain curves for mechanical points which undergo same mean strain-rate during the test clearly chopped-off some large stress values. The curves reveals nevertheless, especially at 266 $s^{-1}$, a slight decrease of stress.

To make the comparison more quantitative, Figure 16b presents the discrepancy between DDI results and modified Krupkowski model predictions. As already presented, modified Krupkowski model has been calibrated on literature data and best fit parameters are provided in Table 3. This figure shows that there is a good agreement between the DDI results and the model predictions for strains beyond a percent. As predicted by the digital twin, the discrepancies remain between $\pm$ 5 % in the plastic regime. Notice that discrepancies for low strains ($<$ 1 %) are also partly due to the fact that the Krupkowski model is not made for describing the elastic regime but only the plastic flow. Finally, this figure demonstrates the ability of the DDI to capture and characterize the rate-dependency of the considered materials from about 10 to 250 $s^{-1}$ using a single test.

## 6. Conclusions and perspectives

In this paper, an emerging full-field inverse stress identification framework, named Data-Driven Identification, is presented. Its recently developed rate-dependent formulation is deployed for the first time to experimentally characterize strain-rate dependence of an elasto-visco-plastic material. Its accuracy, within the framework of a monotonic heterogeneous dynamic test, has been assessed using a digital twin. Then, a pre-notched sample with a central hole has been subjected to a high speed tensile test. Full-field kinematic data have been retrieved using High spatial Resolution Ultra High Speed imaging and Digital Image Correlation. At last, these kinematic fields combined with load measurements have been used as input for the DDI method to estimate stress fields during the experiment and to characterize the material rate-dependence. The main conclusions are as follows:

- The user parameters of the DDI method play an important role in the stress reconstruction. A proper analysis performed on a digital twin can rationalize the selection of these parameters.
- The digital twin evidences the ability of the proposed methodology to retrieve the material response and its rate-dependence despite the use of an arbitrary initialization. Initializing the DDI at zero is also possible (not presented in the document) but affects the convergence especially for highly non-linear behaviors like elasto-visco-plastic responses.
- Using the results from Virtual Image Deformation, the impact of imaging setup noise on the stress estimation can be assessed. An accuracy of $10\,\%^{\pm 5}$ is obtained on the stress estimation (beyond 50 MPa). It falls below 5 % in plastic regime. At last, averaging data to build iso-strain-rate curves allows for identifying the strain-rate dependence within 5 % of

error. Such results are strongly dependent on the sample geometry, DIC parameters, camera and optics used. In this work, a multi-sensor Cordin-580 is considered. Such technology allows high spatial image resolution at ultra high speed at a cost of strong image distortions and sensor noise. In that context, presented experimental uncertainties must be seen as upper bounds and may be significantly reduced if new technologies for high spatial resolution ultra high speed imaging are developed in the market.

- The application of the proposed method to experimental data allows estimating stress fields during non statistically determinate experiments.

- Eventually, the complex non-linear, rate-dependence of the yield stress and hardening flow naturally appears from the data without having to write *a priori* the exact form of the constitutive equation contrary to standard parametric inverse methods. The identified material response, from 10 to 250 $s^{-1}$ in a single test, is consistent with literature data.

DDI comes as a new brick within the experimentalist toolbox for both, local stress probing in the case of non-homogeneous loading case scenarios (*e.g.* local critical stress at fracture onset, flow stress during plastic instabilities, mechanical response of inclusions), and for material characterization. In the latter, as for more standard inverse methods, such as VFM or FEMU, DDI allows to make use of non statistically determinate configurations to characterize material behavior in a more efficient way but also over wider loading conditions domain. Its singularity relies in the fact that no *a priori* knowledge regarding the material constitutive equation is required which allows for, not only identifying parameters, but eventually the form of the constitutive equation itself in situations, especially dynamics, where strong couplings, instabilities, microstructural transformations make the constitutive equation unknown. We do believe, in a near future, that coupling topological optimization, DIC, DDI and deep-learning methods would allow for developing complex models, covering real case loading scenarios, in a record time.

## Acknowledgements

The support of Région Pays de la Loire, Nantes Métropole and European Union through grant Connect Talent IDS is gratefully acknowledged. The support of ANR through grant ANR-16-CE30-0007-01 is also gratefully acknowledged. Finally the authors would like to acknowledge all the colleagues and PhD students contributing to the informal working group, *OutLaw*, at GeM, especially Adrien Leygue and Raphael Langlois for the fruitfull discussions and their recent developments in rate-dependent *DDI*.



## References

[1] M. Badaloni et al. "Impact of Experimental Uncertainties on the Identification of Mechanical Material Properties using DIC". In: *Experimental Mechanics* 55.8 (Oct. 2015), pp. 1411–1426.

[2] B. Barroqueiro et al. "Design of mechanical heterogeneous specimens using topology optimization". In: *International Journal of Mechanical Sciences* 181 (2020), p. 105764.

[3] G. Besnard et al. "Analysis of image series through global digital image correlation". In: *The Journal of Strain Analysis for Engineering Design* 47.4 (2012), pp. 214–228.

[4] P. Bouda et al. "A computational approach to design new tests for viscoplasticity characterization at high strain-rates". In: *Computanional Mechanics* 64.6 (Dec. 2019), pp. 1639–1654.

[5] B. C. Cameron and C. Tasan. "Full-field stress computation from measured deformation fields: A hyperbolic formulation". In: *Journal of the Mechanics and Physics of Solids* 147 (Feb. 2021), p. 104186.

[6] L. Chamoin et al. "Coupling between topology optimization and digital image correlation for the design of specimen dedicated to selected material parameters identification". In: *International Journal of Solids and Structures* 193-194 (June 2020), pp. 270–286.

[7] M. Dalémat et al. "Measuring stress field without constitutive equation". In: *Mechanics of Materials* 136 (Sept. 2019), p. 103087.

[8] M. Dalémat et al. "Robustness of the Data-Driven Identification algorithm with incomplete input data". In: *Journal of Theoretical, Computational and Applied Mechanics* (Feb. 2024).

[9] R. Eggersmann et al. "Model-Free Data-Driven inelasticity". In: *Computer Methods in Applied Mechanics and Engineering* 350 (June 2019), pp. 81–99.

[10] L. Fletcher and F. Pierron. "The Image-Based Inertial Release (IBIR) Test: A New High Strain Rate Test for Stiffness Strain-Rate Sensitivity Identification". In: *Experimental Mechanics* 60.4 (Apr. 2020), pp. 493–508.

[11] L. Fletcher and F. Pierron. "An image-based inertial impact (IBII) test for tungsten carbide cermets". In: *Journal of Dynamic Behavior of Materials* 4.4 (2018), pp. 481–504.

[12] L. Fletcher et al. "High strain rate elasto-plasticity identification using the image-based inertial impact (IBII) test part 1: Error quantification". en. In: *Strain* 57.2 (Apr. 2021).

[13] G. Gary and W. K. Nowacki. "Essai de cisaillement plan appliqué à des tôles minces". fr. In: *Journal de Physique IV* 04.C8 (Sept. 1994), pp. C8–65–C8–70.

[14] G. Haugou, E. Markiewicz, and J. Fabis. "On the use of the non direct tensile loading on a classical split Hopkinson bar apparatus dedicated to sheet metal specimen characterisation". en. In: *International Journal of Impact Engineering* 32.5 (May 2006), pp. 778–798.

[15] J. H. Hollomon. "Tensile deformation". In: *Transactions of the Metallurgical Society of AIME* 12.4 (1945), pp. 1–22.

[16] E. Jones et al. "Parameter covariance and non-uniqueness in material model calibration using the Virtual Fields Method". en. In: *Computational Materials Science* 152 (Sept. 2018), pp. 268–290.

[17] T. Kirchdoerfer and M. Ortiz. "Data Driven Computing with noisy material data sets". In: *Computer Methods in Applied Mechanics and Engineering* 326 (Nov. 2017), pp. 622–641.

[18] T. Kirchdoerfer and M. Ortiz. "Data-driven computational mechanics". In: *Computer Methods in Applied Mechanics and Engineering* 304 (June 2016), pp. 81–101.

[19] R. Langlois, M. Coret, and J. Réthoré. "Non-parametric stress field estimation for history-dependent materials: Application to ductile material exhibiting Piobert–Lüders localization bands". In: *Strain* (2022), e12410.

[20] B. Langrand and A. Combescure. "Non-linear and failure behaviour of spotwelds: a "global" finite element and experiments in pure and mixed modes I/II". en. In: *International Journal of Solids and Structures* 41.24-25 (Dec. 2004), pp. 6631–6646.

[21] B. Langrand and E. Markiewicz. "Strain-rate dependence in spot welds: Non-linear behaviour and failure in pure and combined modes I/II". en. In: *International Journal of Impact Engineering* 37.7 (July 2010), pp. 792–805.

[22] A. Leygue et al. "Data-based derivation of material response". In: *Computer Methods in Applied Mechanics and Engineering* 331 (Apr. 2018), pp. 184–196.

[23] A. Leygue et al. "Non-parametric material state field extraction from full field measurements". In: *Computunational Mechanics* 64.2 (Aug. 2019), pp. 501–509.

[24] C. Liu. "Nonuniform Stress Field Determination Based on Deformation Measurement". In: *Journal of Applied Mechanics* 88.7 (July 2021), p. 071005.

[25] J. MacQueen et al. "Some methods for classification and analysis of multivariate observations". In: *Proceedings of the fifth Berkeley symposium on mathematical statistics and probability*. Vol. 1. 14. Oakland, CA, USA. 1967, pp. 281–297.

[26] É. Markiewicz et al. "A methodology for the viscoplastic behaviour characterisation of spot-weld heat affected materials". en. In: *Journal of Materials Processing Technology* 238 (Dec. 2016), pp. 169–180.

[27] F. Pierron and L. Fletcher. "Generalized Stress–Strain Curves for IBII Tests on Isotropic and Orthotropic Materials". In: *Journal of Dynamic Behavior of Materials* 5.2 (June 2019), pp. 180–193.

[28] F. Pierron, H. Zhu, and C. Siviour. "Beyond Hopkinson's bar". en. In: *Philosophical Transactions of the Royal Society A: Mathematical, Physical and Engineering Sciences* 372.2023 (July 2014), pp. 20130195–20130195.

[29] A. Platzer et al. "Finite element solver for data-driven finite strain elasticity". In: *Computer Methods in Applied Mechanics and Engineering* 379 (June 2021), p. 113756.

[30] D. Priadi et al. "Introduction of strain rate effects in constitutive equations suitable for sheet metal stamping applications". In: *MECAMAT 91*. 1991, p. 1991.

[31] J. Réthoré. *UFreckles, doi:10.5281/zenodo.1433776*. Oct. 2018.

[32] M. Rossi et al. "Effect of DIC Spatial Resolution, Noise and Interpolation Error on Identification Results with the VFM: Effect of DIC Spatial Resolution, Noise and Interpolation on VFM Identification". In: *Strain* 51.3 (June 2015), pp. 206–222.

[33] M. Rossi et al. "A procedure for specimen optimization applied to material testing in plasticity with the virtual fields method". In: *AIP Conference Proceedings*. ESAFORM 2016: Proceedings of the 19th International ESAFORM Conference on Material Forming. AIP Publishing LLC. Nantes, France, 2016, p. 200016.

[34] R. Seghir and F. Pierron. "A Novel Image-based Ultrasonic Test to Map Material Mechanical Properties at High Strain-rates". en. In: *Experimental Mechanics* 58.2 (Feb. 2018), pp. 183–206.

[35] L. Stainier, A. Leygue, and M. Ortiz. "Model-free data-driven methods in mechanics: material data identification and solvers". In: *Compututational Mechanics* 64.2 (Aug. 2019), pp. 381–393.

[36] H. W. Swift. "Plastic instability under plane stress". In: *Journal of the Mechanics and Physics of Solids* 1.1 (1952), pp. 1–18.

[37] G. Valdés-Alonzo et al. "Phase distribution and properties identification of heterogeneous materials: A data-driven approach". In: *Computer Methods in Applied Mechanics and Engineering* 390 (2022), p. 114354.

[38] A. Vinel. "Characterization of the thermomechanical behaviour of metals for high strain-rates, using ultrahigh speed imaging cameras". Theses. École centrale de Nantes, Jan. 2022.

[39] A. Vinel et al. "Metrological assessment of multi-sensor camera technology for spatially-resolved ultra-high-speed imaging of transient high strain-rate deformation processes". In: *Strain* 57.4 (2021), e12381.

[40] J.-F. Witz et al. "Digital image correlation for large strain". In: *International Digital Imaging Correlation Society*. Springer, 2017, pp. 163–167.

[41] R.-C. Yang. "A regularized finite-element digital image correlation for irregular displacement field". In: *Optics and Lasers in Engineering* 56 (2014), pp. 67–73.